

## Atomic-scale cellular model and profile simulation of poly-Si gate etching in high-density chlorine-based plasmas: Effects of passivation layer formation on evolution of feature profiles

Yugo Osano and Kouichi Ono

Citation: *Journal of Vacuum Science & Technology B* **26**, 1425 (2008); doi: 10.1116/1.2958240

View online: <http://dx.doi.org/10.1116/1.2958240>

View Table of Contents: <http://scitation.aip.org/content/avs/journal/jvstb/26/4?ver=pdfcov>

Published by the AVS: Science & Technology of Materials, Interfaces, and Processing

### Articles you may be interested in

[Poly- Si / TiN / Mo / HfO<sub>2</sub> gate stack etching in high-density plasmas](#)

*J. Vac. Sci. Technol. B* **29**, 011024 (2011); 10.1116/1.3533939

[Feature profile evolution during shallow trench isolation etch in chlorine-based plasmas. II. Coupling reactor and feature scale models](#)

*J. Vac. Sci. Technol. B* **26**, 1919 (2008); 10.1116/1.2998759

[Modeling of fluorine-based high-density plasma etching of anisotropic silicon trenches with oxygen sidewall passivation](#)


*J. Appl. Phys.* **94**, 6311 (2003); 10.1063/1.1621713





[Level set approach to simulation of feature profile evolution in a high-density plasma-etching system](#)

*J. Vac. Sci. Technol. B* **19**, 701 (2001); 10.1116/1.1370174

[Plasma-induced nitridation of gate oxide dielectrics: Linked equipment-feature atomic scale simulations](#)

*J. Vac. Sci. Technol. A* **17**, 1356 (1999); 10.1116/1.581820


Instruments for Advanced Science

<p>Contact Hiden Analytical for further details:  <b>W</b> <a href="http://www.HidenAnalytical.com">www.HidenAnalytical.com</a>  <b>E</b> <a href="mailto:info@hiden.co.uk">info@hiden.co.uk</a></p> <p><a href="#">CLICK TO VIEW</a> our product catalogue</p>	 <p><b>Gas Analysis</b></p> <ul style="list-style-type: none"> <li>› dynamic measurement of reaction gas streams</li> <li>› catalysis and thermal analysis</li> <li>› molecular beam studies</li> <li>› dissolved species probes</li> <li>› fermentation, environmental and ecological studies</li> </ul>	 <p><b>Surface Science</b></p> <ul style="list-style-type: none"> <li>› UHV TPD</li> <li>› SIMS</li> <li>› end point detection in ion beam etch</li> <li>› elemental imaging - surface mapping</li> </ul>	 <p><b>Plasma Diagnostics</b></p> <ul style="list-style-type: none"> <li>› plasma source characterization</li> <li>› etch and deposition process reaction</li> <li>› kinetic studies</li> <li>› analysis of neutral and radical species</li> </ul>	 <p><b>Vacuum Analysis</b></p> <ul style="list-style-type: none"> <li>› partial pressure measurement and control of process gases</li> <li>› reactive sputter process control</li> <li>› vacuum diagnostics</li> <li>› vacuum coating process monitoring</li> </ul>
---	--	--	--	--

# Atomic-scale cellular model and profile simulation of poly-Si gate etching in high-density chlorine-based plasmas: Effects of passivation layer formation on evolution of feature profiles

Yugo Osano<sup>a)</sup> and Kouichi Ono<sup>b)</sup>

Department of Aeronautics and Astronautics, Graduate School of Engineering, Kyoto University, Yoshida-Honmachi, Sakyo-ku, Kyoto 606-8501, Japan

(Received 8 February 2008; accepted 24 June 2008; published 15 August 2008)

Atomic-scale cellular model has been developed to simulate the feature profile evolution during poly-Si gate etching in high-density  $\text{Cl}_2$  and  $\text{Cl}_2/\text{O}_2$  plasmas, with emphasis being placed on the formation of passivation layers on feature surfaces. The model took into account the behavior of  $\text{Cl}^+$  ions, Cl and O neutrals, and etch products and byproducts of  $\text{SiCl}_x$  and  $\text{SiCl}_x\text{O}_y$  in microstructural features. The transport of ions and neutrals in microstructures and in substrates was analyzed by the two-dimensional Monte Carlo calculation with three velocity components. The surface chemistry included ion-enhanced etching, chemical etching, and passivation layer formation through surface oxidation and deposition of etch products and byproducts. The computational domain was taken to consist of two-dimensional square cells or lattices of atomic size, and the evolving interfaces were represented by removing Si atoms from and/or allocating them at the cells concerned. Calculations were performed for different line-and-space pattern features of down to 30 nm space width, with an incoming ion energy, ion flux, and neutral reactant-to-ion flux ratio of  $E_i=50$  eV,  $\Gamma_i^0=1.0 \times 10^{16}$   $\text{cm}^{-2}$   $\text{s}^{-1}$ , and  $\Gamma_n^0/\Gamma_i^0=10$ . Numerical results reproduced the evolution of feature profiles, critical dimensions, and their microscopic uniformity (or aspect-ratio dependence) on nanometer scale, depending on substrate temperature, incoming flux of oxygen and etch byproducts, and sticking probability of etch products and byproducts on feature surfaces: the lateral etching on sidewalls is suppressed by surface oxidation thereon. The oxidation also reduces the etch rate on bottom surfaces, leading to a transition from regular to inverse reactive ion etching (RIE) lag with increasing flux of oxygen; in practice, the RIE lag remains almost unchanged for narrow space features owing to reduced oxygen fluxes thereinto, thus leading to regular and inverse RIE lags coexistent in a series of different pattern features. The deposition or redeposition of etch products (desorbed from feature surfaces) onto sidewalls results in the sidewall tapering, which is more significant for narrower space features; in contrast, the deposition of byproducts (coming from the plasma) onto sidewalls results in the tapering, which is more significant for wider features. Synergistic effects between the deposition of etch products/byproducts and surface oxidation enhance the passivation layer formation on feature surfaces, which in turn increases the sidewall tapering and the degree of regular and inverse RIE lags depending on feature width. The present model also enabled the authors to simulate the surface reaction multilayers and passivation layers on atomic scale, along with their chemical constituents and surface roughness. © 2008 American Vacuum Society. [DOI: 10.1116/1.2958240]

## I. INTRODUCTION

Chlorine-based plasmas are widely employed for the etching of poly-Si gate electrodes of microelectronic devices, where a small amount of  $\text{O}_2$  is often added to improve the etched profile and the selectivity over thin gate oxides. It is generally appreciated that in high-density  $\text{Cl}_2/\text{O}_2$  and  $\text{Cl}_2/\text{HBr}/\text{O}_2$  plasmas, the etched profile, critical dimension (CD), and their microscopic uniformity (or aspect-ratio dependence) are significantly influenced by the formation of passivation layers on feature surfaces,<sup>1</sup> through deposition of etch products/byproducts and surface oxidation during etch-

ing. In practice, etch products come directly from feature surfaces, and byproducts from the plasma; the oxygen originates from plasma chamber walls and windows of aluminum oxides or quartz as well as from additive oxygen. In particular, passivation layers on feature sidewalls suppress the lateral etching and reduce the undercutting beneath the mask, and the excess deposition results in outwardly tapered profiles. Such sidewall profiles lead to the CD loss/gain of gate electrodes, which in turn closely affects the transistor channel length and so the device performance. Thus, a deeper understanding of plasma-surface interactions responsible for passivation layer formation during etching is increasingly important for nanometer-scale control of the etched profile, CD, and their microscopic uniformity of gate electrodes, as integrated circuit device dimensions continue to be scaled down to much less than 100 nm.<sup>1</sup>

<sup>a)</sup>Present address: Core Technology Center, Nikon Corporation, 1-10-1 Asamizodai, Sagamihara-shi, Kanagawa 228-0828, Japan; electronic mail: yugo.o@nikon.co.jp

<sup>b)</sup>Electronic mail: ono@kuaero.kyoto-u.ac.jp

A number of experiments have been performed to investigate the formation of passivation layers during Si etching in high-density chlorine-based plasmas. Guinn *et al.* examined the chemical constituents and concentrations on sidewalls and bottom surfaces of poly-Si electrodes etched in  $\text{Cl}_2$  and  $\text{Cl}_2/\text{O}_2$  plasmas, by using x-ray photoelectron spectroscopy (XPS);<sup>2,3</sup> they found that  $\text{SiCl}_x\text{O}_y$  layers are formed on feature surfaces, where the O coverage is much larger on sidewalls than on bottom surfaces. Bell and Joubert also performed the XPS analysis of feature surfaces of poly-Si electrodes etched in  $\text{Cl}_2$  and  $\text{Cl}_2/\text{HBr}/\text{O}_2$  plasmas, showing that the passivation layers formed on sidewalls are chlorine-rich silicon oxide films.<sup>4,5</sup> Nishikawa *et al.* investigated *in situ* Fourier transform infrared spectra in the gas phase and on substrate surfaces during  $\text{Cl}_2$  plasma etching of Si;<sup>6</sup> they indicated that in the gas phase, there are etch byproducts such as silicon oxides  $\text{SiO}_y$  and oxychlorides  $\text{SiCl}_x\text{O}_y$ , along with primary etch products of silicon tetrachlorides  $\text{SiCl}_4$ , and that the etch byproducts strongly affect the etch rates and etched profiles. However, the origin of passivation layers is not fully understood because the transport and surface chemistry of ions and neutrals including etch products and byproducts is difficult to observe in microstructural features.

Feature profile simulations have also been developed to analyze the influences of complex surface reaction processes that occur. The simulation model often took into account the deposition or redeposition of etch products  $\text{SiCl}_4$  within the feature, deposition of etch byproducts  $\text{SiCl}_2$  coming from the plasma, and surface oxidation, in addition to ion-enhanced etching; the string model<sup>7,8</sup> and the cell removal method<sup>9-11</sup> were then used along with Langmuir adsorption kinetics to represent the evolving interfaces through surface reactions. However, these simulations did not take into account synergistic effects of surface oxidation and deposition; moreover, the substrates were represented as a continuum with monolayer adsorption and reaction kinetics on surfaces, and so atomistic processes on nanometer scale were hard to be treated including surface reaction multilayers as well as passivation layers. On the other hand, molecular dynamics (MD) simulations have recently been developed to clarify surface reaction processes on atomic scale, giving the etching characteristics such as etch yield, stoichiometry of etch products, and microscopic surface structures during etching.<sup>12-15</sup> However, few MD studies have treated the deposition of etch products/byproducts and surface oxidation; moreover, the feature profile evolution is also still difficult for the MD simulation to deal with, owing to an enormous number of particles and their interactions to be taken into account in the simulation.

In this article, we present an atomic-scale cellular model and feature profile simulation for poly-Si gate etching in high-density  $\text{Cl}_2$  and  $\text{Cl}_2/\text{O}_2$  plasmas, with emphasis being placed on the formation of passivation layers on feature surfaces during etching. The model is based on our previous atomic-scale model for the ion-enhanced etching,<sup>16,17</sup> taking into account not only  $\text{Cl}^+$  ions and Cl neutrals but also O neutrals and etch products/byproducts of  $\text{SiCl}_x$  and  $\text{SiCl}_x\text{O}_y$

in microstructural features. The simulation domain is taken to consist of a number of square cells or lattices of atomic size, and the evolving interfaces are represented by removing Si atoms from and/or allocating them at the cells concerned. The transport of ions and neutrals in microstructures and in substrates is analyzed by a particle simulation or the Monte Carlo calculation. The surface chemistry includes ion-enhanced etching, chemical etching, surface oxidation, deposition or redeposition of etch products within the feature, and deposition of etch byproducts coming from the plasma; the passivation layers are assumed to be formed through surface oxidation and deposition of etch products and byproducts, being sputtered or removed under ion bombardment.

The present atomic-scale cellular model gives us a deeper understanding of plasma-surface interactions during etching, for nanometer-scale control of the etched profiles, CDs, and their microscopic uniformity, along with the atomic-scale view of reaction multilayers, passivation layers, their chemical constituents, and surface roughness. In practice, the present model can simulate the evolution of feature profiles, CDs, and their microscopic uniformity during plasma etching on atomic or nanometer scale; the model is also capable of simulating the surface roughening and/or residues primarily caused by micromasks formed through stochastically localized surface oxidation during etching, which are difficult or impossible to model by using previous methods published.<sup>7-11</sup> The structure and chemical constituents of reaction and passivation layers on feature sidewalls and bottom surfaces, which are also difficult to simulate by previous methods,<sup>7-11</sup> would also be helpful in understanding what occurs in microstructural features during etching and what is responsible for the processing achieved.

The next section describes the model for surface chemistry and profile simulation. Numerical results are then given in Sec. III for the feature profile evolution during etching. Calculations are performed for different line-and-space pattern features of down to 30 nm space width as a function of substrate temperature, incoming flux of oxygen and etch byproducts from the plasma, and sticking probability of etch products and byproducts on feature surfaces. The profile evolution and microscopic uniformity are investigated with attention being given to reactive ion etching (RIE) lag, inverse RIE lag, and profile anomalies such as undercutting, bowing, and tapering. Finally, Sec. IV gives conclusions of this article.

## II. MODEL

We consider a two-dimensional structure or an infinitely long trench being etched. The substrates are taken to consist of cells or lattices of atomic size, and the evolving interfaces are modeled by the so-called cell removal method, as in our previous study.<sup>17</sup> The present atomic-scale cellular model, which is a phenomenological model at an intermediate between the MD simulation and continuum models, gives a nanometer-scale representation of the feature profile evolu-

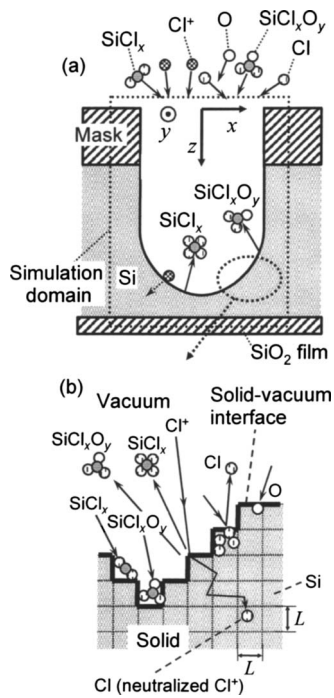


FIG. 1. (a) Schematic illustration of the geometry of an infinitely long trench of Si being etched, together with the simulation domain and coordinate system presently employed. Here,  $\text{Cl}^+$  ions, Cl neutrals, O neutrals, and etch byproducts of silicon chlorides  $\text{SiCl}_x$  and oxychlorides  $\text{SiCl}_x\text{O}_y$  are injected from the top of the simulation domain with three velocity components ( $v_x, v_y, v_z$ ); moreover, etch products such as  $\text{SiCl}_x$  and  $\text{SiCl}_x\text{O}_y$  are desorbed or sputtered from feature surfaces during etching. The ions are taken to be injected into the simulation domain almost vertically with a given energy and angular distribution, while the neutrals are injected thermally with an isotropic velocity distribution. The etch products are assumed to be desorbed thermally or removed randomly from the surfaces being etched according to the so-called cosine law. The simulation domain concerned (solid/substrate and vacuum) in a two-dimensional space ( $x, z$ ) is divided into square cells or lattices of atomic size  $L = \rho_{\text{Si}}^{-1/3} = 2.7 \text{ \AA}$  with  $\Delta y = L$  taken in the  $y$  direction, as partly shown in (b), where  $\rho_{\text{Si}} = 5.0 \times 10^{22} \text{ cm}^{-3}$  is the atomic density of Si substrates, and Si atoms are allocated at the respective cells concerned.

tion during etching along with reaction and passivation layers on feature surfaces, their chemical constituents, and surface roughness.

Figure 1(a) illustrates the simulation domain with the coordinate system ( $x, z$ ) presently employed, where  $\text{Cl}^+$  ions, Cl neutrals, O neutrals, and etch byproducts of silicon chlorides  $\text{SiCl}_x$  and oxychlorides  $\text{SiCl}_x\text{O}_y$  are taken to be injected from the plasma into microstructural features on substrates; moreover, etch products such as  $\text{SiCl}_x$  and  $\text{SiCl}_x\text{O}_y$  are desorbed or sputtered from the feature surfaces during etching. The simulation domain concerned is divided into two-dimensional square cells or lattices of  $L = \rho_{\text{Si}}^{-1/3} = 2.7 \text{ \AA}$ , with  $\Delta y = L$  taken in the  $y$  direction, as partly shown in Fig. 1(b), where  $\rho_{\text{Si}} = 5.0 \times 10^{22} \text{ cm}^{-3}$  is the atomic density of Si substrates, and Si atoms are allocated in the respective cells of substrates. The cell or lattice is assumed to be rigid, and Si atoms are taken to be removed from the outermost surface cells when the etching causes the desorption of reaction products  $\text{SiCl}_x$  and the sputtering causes the removal of

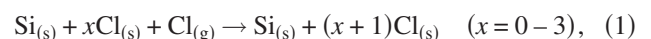
oxygen-containing products  $\text{SiCl}_x\text{O}_y$ ; in contrast, Si atoms are newly allocated at the cells concerned when the deposition of etch products/byproducts occurs.

The transport of ions and neutrals in microstructures onto feature surfaces is analyzed by the two-dimensional particle simulation based on successively injected single-particle trajectories with three velocity components ( $v_x, v_y, v_z$ ), and the Monte Carlo calculation is employed for the trajectory of ions that penetrate into substrates on incidence.<sup>17</sup> In practice, the  $\text{Cl}^+$ , Cl, O,  $\text{SiCl}_x$ , and  $\text{SiCl}_x\text{O}_y$  are randomly allocated at the top boundary of the simulation domain, being successively injected therefrom according to given energies, angular distributions, and fluxes. The particles are assumed to move straight in microstructures without collision with other particles therein, where the transport is calculated every movement of the approximate atomic separation  $L$ . If there is a Si atom at any of the four sites neighboring to the cell or lattice where the particle is located, it is assumed to reach the surface. Note that the ions incident on surfaces are known to be neutralized thereon owing to the Auger process, and so the feature surfaces are taken to be charge neutral during etching.

## A. Ion-enhanced etching

The model for neutral adsorption and ion-enhanced etching has been detailed in our previous paper.<sup>17</sup> Briefly,  $\text{Cl}^+$  ions are injected into the simulation domain with a given energy incident on substrate surfaces after being accelerated through the sheath; the incident angle is given by randomly sampling from the angular distribution of ion fluxes, which depends on the ratio  $R = E_i/kT_i$  of the incident ion energy  $E_i$  to the ion temperature  $kT_i$ .<sup>7,8,17,18</sup> Energetic ions are taken to penetrate into substrates, stop at a finite depth, and react with substrate atoms thereat; the trajectory and stopping of  $\text{Cl}^+$  ions in Si is also analyzed by the two-dimensional particle simulation (or the Monte Carlo calculation), including their scattering at every collision with a Si atom in the cell or lattice.<sup>19</sup> The penetration of energetic  $\text{Cl}^+$  ions into Si causes the multilayer adsorption of Cl, thus resulting in surface reaction multilayers of  $\text{SiCl}_x$ , as indicated by the MD simulation.<sup>12–15</sup>

Neutral reactants of Cl are injected thermally with an isotropic velocity distribution; the incident angle is given by randomly sampling from the so-called cosine distribution. In contrast to ions, neutrals have too small energy to penetrate into substrates, and so the neutral adsorption occurs only on the outermost surfaces (or at the outermost surface cells or lattices). The sticking coefficient or probability of Cl on Si is known to be  $S_{\text{Cl}} \approx 0.7$ ,<sup>20,21</sup> while the dissociative adsorption of  $\text{Cl}_2$  molecules is known to be  $S_{\text{Cl}_2} \approx 0.55$ .<sup>22,23</sup> In practice, for simplicity, Cl neutrals are assumed to adsorb or stick on unsaturated surfaces of Si with a probability  $S_n = 1$ ,

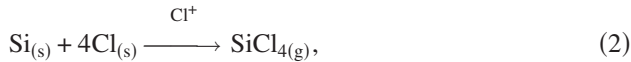


where (s) and (g) represent the surface and the gas phase, respectively. On the other hand, they are re-emitted thermally or reflected randomly on saturated surfaces, which then



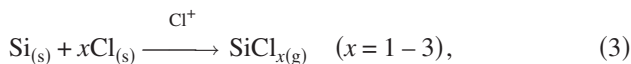
move towards another surfaces of the feature or go out of the simulation domain.

In the calculation, the ion-enhanced etching or the removal of substrate Si atoms is assumed to occur on the outermost surfaces with the cells being chlorine saturated; in practice, the saturated silicon chlorides  $\text{SiCl}_4$  are taken to be desorbed from the surface through ion bombardment, with the reaction being



where  $\text{Cl}^+$  above the arrow indicates the reaction induced by energetic ion bombardment. The etching reaction is taken to occur with a probability corresponding to the etch yield  $Y_{\text{Si/Cl}^+}$  (the number of substrate atoms etched per incident ion on saturated surfaces), depending on the incident ion energy  $E_i$  and angle  $\theta$  on surfaces. In practice, the functional form  $Y_{\text{Si/Cl}^+} = C(\sqrt{E_i} - \sqrt{E_{\text{th}}})f(\theta)$  is employed in this study with a constant  $C=0.77$  and a threshold energy  $E_{\text{th}}=20$  eV, which were determined from the experimental etch yields for  $\text{Cl}^+$  ions on Si surfaces chlorine saturated;<sup>24</sup> moreover, the angular dependence is taken to be  $f(\theta)=1$  for  $\theta < \theta_{\text{cr}}$  and  $=\cos \theta / \cos \theta_{\text{cr}}$  for  $\theta > \theta_{\text{cr}}$ , with the critical angle being  $\theta_{\text{cr}}=45^\circ$ . Note that for  $Y_{\text{Si/Cl}^+} > 1$ , Si atoms are assumed to be further removed with a probability  $(Y_{\text{Si/Cl}^+} - 1)$  from the neighbor surface cells saturated.<sup>17</sup> In calculating the incident angle  $\theta$  on feature surfaces, the direction of the surface normal is represented by the four-point technique, where the surface normal is determined by the presence/absence of four neighboring cells concerned.<sup>17</sup>

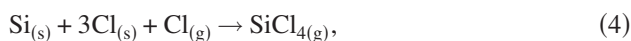
In addition, the ion-enhanced etching is also taken to occur on the outermost surfaces unsaturated,



with a probability corresponding to the yield  $Y'_{\text{Si/Cl}^+} = (x/4)Y_{\text{Si/Cl}^+}$ . However, the sputtering of Si atoms through  $\text{Cl}^+$  ion bombardment on unchlorinated surfaces is neglected in this study, owing to the yield about an order of magnitude small.<sup>25</sup>

## B. Spontaneous chemical etching

Neutral reactants of Cl incident on Si surfaces lead to spontaneous or purely chemical etching, which is assumed to occur on the outermost surfaces being chlorine saturated. The etching reaction is taken to occur through an incidence of Cl neutrals as



with a probability corresponding to the reaction probability  $\alpha_{\text{Si/Cl}}$  (the number of substrate atoms etched per incident reactant under saturated surface conditions), which is calculated from the experiments of Ogryzlo *et al.*<sup>26</sup> They measured the chemical etch rate  $ER_{\text{chem}}$  for Si in heated  $\text{Cl}_2$  gases as a function of dopant concentration  $N_e$ , Cl concentration  $n_{\text{Cl}}$  in the gas phase, and surface temperature  $T_s$ ,

$$ER_{\text{chem}} = \nu N_e^\gamma n_{\text{Cl}} T_s^{1/2} \exp(-E/kT_s), \quad (5)$$

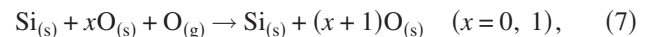
where  $\nu=4.04 \times 10^{-18} \text{ \AA cm}^{3(1+\gamma)} \text{ min}^{-1} \text{ K}^{-1/2}$ ,  $\gamma=0.39$ , and  $E=4.7$  kcal/mol are constants determined for P-doped poly-Si, and  $k$  is the Boltzmann constant. The probability  $\alpha_{\text{Si/Cl}}$  is then given by

$$\alpha_{\text{Si/Cl}} = \frac{\rho_{\text{Si}} ER_{\text{chem}}}{\Gamma_{\text{Cl}}} = 4\rho_{\text{Si}} \frac{\nu N_e^\gamma T_s^{1/2} \exp(-E/kT_s)}{\bar{u}}, \quad (6)$$

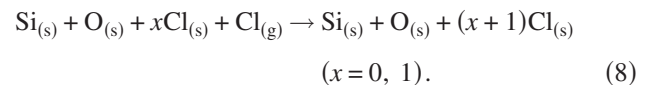
where  $\Gamma_{\text{Si}} = \rho_{\text{Si}} ER_{\text{chem}}$  is the flux of Si atoms desorbed from the surface through purely chemical etching,  $\Gamma_{\text{Cl}} = (1/4)n_{\text{Cl}}\bar{u}$  is the flux of Cl atoms incident on surfaces, and  $\bar{u} = \sqrt{8kT_g/\pi m_{\text{Cl}}}$  is the average thermal velocity of Cl atoms with  $m_{\text{Cl}}$  being the atomic mass concerned.<sup>27</sup> The dopant concentration is taken to be  $N_e=1.0 \times 10^{20} \text{ cm}^{-3}$  in this study, with a gas temperature  $T_g=500$  K.

## C. Surface oxidation

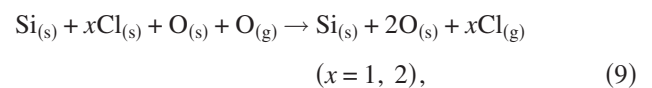
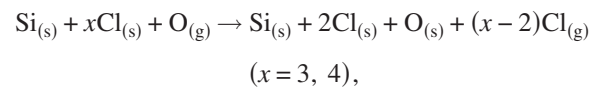
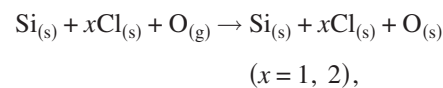
Surface oxidation is taken to be induced by adsorption of neutral O atoms on the outermost surfaces, where the injection and transport of O atoms in microstructural features is treated similarly to that of Cl neutrals. The sticking coefficient or probability of O on Si is known to be  $S_{\text{O}} \approx 1$ ,<sup>28</sup> in contrast, the dissociative adsorption of  $\text{O}_2$  molecules is neglected owing to a small probability  $S_{\text{O}_2} < 0.01$ .<sup>29</sup> It is noted that the adsorption of a maximum of two O atoms is allowed with a probability  $S_{\text{O}}=1$  at a surface cell or lattice containing Si to form  $\text{SiO}_y$ ,



while O atoms are re-emitted thermally or reflected randomly on saturated surfaces with O. Similarly, Cl atoms are taken to adsorb or stick on unsaturated surfaces with a probability  $S_n=1$ ,



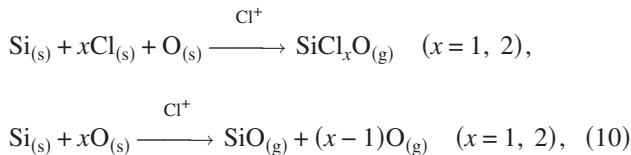
Moreover, strongly reactive O neutrals are assumed to oxidize  $\text{SiCl}_x$  and  $\text{SiCl}_x\text{O}_y$  surfaces ( $x+2y \leq 4$ ) with a probability of unity,<sup>30,31</sup>



where the latter two result in desorption or emission of displaced Cl atoms from the surface. It is further assumed that there is no reduction of O on oxidized  $\text{SiO}_y$  and  $\text{SiCl}_x\text{O}_y$  surfaces by incidence of Cl neutrals, or by the reverse reaction of the latter two in Eq. (9), owing to the Si–O bond

relatively strong as compared to that of Si–Cl; thus, Cl neutrals are usually reflected on saturated SiO<sub>2</sub> and SiCl<sub>2</sub>O surfaces on incidence. In addition, no spontaneous chemical etching is taken to be induced by Cl neutrals incident on oxidized surfaces.

The etching or removal of oxidized surfaces is given by



where silicon oxides SiO<sub>y</sub> and oxychlorides SiCl<sub>x</sub>O<sub>y</sub> are desorbed or removed from the surface by physical sputtering through energetic Cl<sup>+</sup> ion bombardment. The etch or sputter yield for a Cl<sup>+</sup> ion on oxidized surfaces is taken to be smaller than the yield  $Y_{\text{Si/Cl}^+}$  for the ion-enhanced etching as given earlier; in practice,

$$Y_{\text{Si/Cl}^+}^{\text{sp}} = \frac{1}{7}C(\sqrt{E_i} - \sqrt{E_{\text{th}}^{\text{sp}}})g(\theta) \quad (11)$$

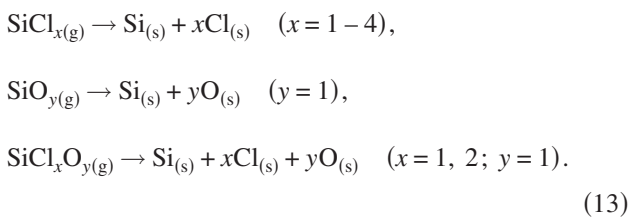
is employed in this study, according to the Si to SiO<sub>2</sub> etch rate ratio  $Y_{\text{Si}}/Y_{\text{SiO}_2} \sim 7$  experimentally obtained for Ar<sup>+</sup> ions with an energy  $E_i = 100$  eV at normal incidence on surfaces in Cl<sub>2</sub> environments.<sup>32</sup> Here, the constant  $C = 0.77$  is the same as in  $Y_{\text{Si/Cl}^+}$ , while the threshold energy is taken to be  $E_{\text{th}}^{\text{sp}} = 30$  eV ( $> E_{\text{th}}$ ), and the angular dependence

$$g(\theta) = \frac{5}{3}(18.7 \cos \theta - 64.7 \cos^2 \theta + 145.2 \cos^3 \theta - 206 \cos^4 \theta + 147.3 \cos^5 \theta - 39.9 \cos^6 \theta) \quad (12)$$

peaking at  $\theta \sim 65^\circ$  is taken from a model for physical sputtering processes.<sup>10</sup>

#### D. Deposition of etch products and byproducts

Silicon chlorides SiCl<sub>x</sub>, oxides SiO<sub>y</sub>, and oxychlorides SiCl<sub>x</sub>O<sub>y</sub> deposited on feature surfaces consist of etch products coming directly from the surfaces being etched and etch byproducts coming from the plasma, as illustrated in Fig. 2. The etch products are desorbed from feature surfaces through the etching and sputtering processes [Eqs. (2)–(4) and (10)] mentioned above. The products desorbed are assumed to move straight toward another surfaces of the feature in microstructures without collision with other particles therein, and then to stick or redeposit on all feature surfaces of mask as well as Si with a probability  $S_q$ ,



Otherwise, they are re-emitted thermally or reflected randomly with a probability  $(1-S_q)$ , which then move further toward another surfaces of the feature or go out of the simulation domain into the plasma. The sticking coefficient or probability concerned is taken to be in the range  $S_q =$

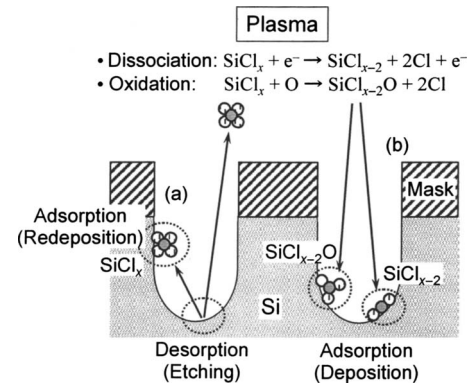
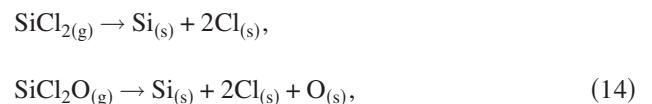


FIG. 2. Schematic of the transport of etch products and byproducts in microstructural features: (a) products desorbed or sputtered from feature surfaces and (b) byproducts coming from the plasma. The etch products such as silicon chlorides SiCl<sub>x</sub> and oxychlorides SiCl<sub>x</sub>O<sub>y</sub> are assumed to be desorbed thermally or removed randomly from the surfaces being etched, move straight toward another surfaces of the feature without collision with other particles therein, and then stick or redeposit on all feature surfaces of mask as well as Si with a probability  $S_q$ ; otherwise, they are re-emitted thermally or reflected randomly from the feature surfaces on incidence with a probability  $(1-S_q)$ , which then move further toward another surfaces of the feature or go out of the simulation domain into the plasma. The etch products coming into the plasma are dissociated by electron impact and/or oxidized by reaction with O atoms therein, a part of which return back to substrate surfaces as etch byproducts. The transport of byproducts in microstructural features is taken to be similar to that of products: the etch byproducts of SiCl<sub>x</sub> and SiCl<sub>x</sub>O<sub>y</sub> move straight toward feature surfaces, and then stick or deposit thereon with a probability  $S_p$ , or are reemitted or reflected therefrom with a probability  $(1-S_p)$ .

0.002–0.1 because saturated SiCl<sub>4</sub> is known to have a small probability of  $S_q \leq 0.002$  (Ref. 33) or  $S_q \approx 0.03$  (Ref. 34) on Si, as compared to  $S_q \approx 0.1-0.5$  for unsaturated SiCl<sub>x</sub>.<sup>6,35</sup>

The etch products coming into the plasma are dissociated by electron impact and/or oxidized by reaction with O atoms therein, a part of which return back to substrate surfaces as etch byproducts and then are transported in microstructures onto feature surfaces. Regarding etch byproducts of SiCl<sub>x</sub> coming from the plasma, SiCl<sub>2</sub> formed by electron-impact dissociation of primary etch products SiCl<sub>4</sub> (Refs. 36 and 37) is taken into account in this study. Etch byproducts of SiO<sub>y</sub> and SiCl<sub>x</sub>O<sub>y</sub> are formed by sputtering of oxidized etch products on chamber walls as well as substrate surfaces, and also by oxidized reaction of SiCl<sub>x</sub> in the plasma.<sup>6</sup> We simply assume that oxygen-containing byproducts coming from the plasma are SiCl<sub>2</sub>O. The etch byproducts concerned are taken to stick or deposit on all feature surfaces with a probability in the range  $S_p = 0.1-0.5$ ,



and the surface re-emission or reflection occurs with a probability  $(1-S_p)$ .

It is generally appreciated that the concentration of etch byproducts in the plasma and thus their flux onto substrate surfaces is significantly decreased during overetch step as compared to during main etch, because of the decreased flux

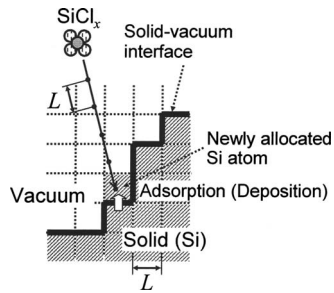


FIG. 3. Schematic of the sticking or deposition of etch products and byproducts on feature surfaces, which is represented by the so-called ballistic deposition model. We examine if there are Si atoms around the etch product/byproduct after every movement of the approximate atomic separation  $L$ ; if there is a Si atom at any of the four sites neighboring to the cell or lattice where the product/byproduct is located, it is assumed to reach the surface and to stick or deposit thereon. Then, a Si atom is newly allocated at the cell concerned, where Cl and O atoms of  $\text{SiCl}_x$ ,  $\text{SiO}_y$ , and  $\text{SiCl}_x\text{O}_y$  are also taken to stick or adsorb simultaneously.

of etch products desorbed from substrate surfaces during overetch. Thus, to take into account the time-varying flux of etch byproducts coming from the plasma, we assume a returning probability  $P_r$ ; in the calculation, byproducts  $\text{SiCl}_2$  and/or  $\text{SiCl}_2\text{O}$  are injected thermally with an isotropic velocity distribution from the top of the simulation domain, with the probability  $P_r$  every after the desorbed products  $\text{SiCl}_x$ ,  $\text{SiO}_y$ , and  $\text{SiCl}_x\text{O}_y$  go out of the simulation domain into the plasma.

To represent the deposition of etch products/byproducts on feature surfaces, the ballistic deposition model<sup>38</sup> is employed, as illustrated in Fig. 3, and the deposition is taken to occur on the outermost surfaces (or at the outermost surface cells or lattices). We examine if there are Si atoms around the etch product/byproduct after every movement of the approximate atomic separation  $L$ ; if there is a Si atom at any of the four sites neighboring to the cell or lattice where the product/byproduct is located, it is assumed to reach the surface and to stick or deposit thereon. Then, a Si atom is newly allocated at the cell concerned, where Cl and O atoms of  $\text{SiCl}_x$ ,  $\text{SiO}_y$ , and  $\text{SiCl}_x\text{O}_y$  are also taken to stick or adsorb simultaneously. The deposition of etch products/byproducts is treated similarly on mask feature surfaces as well as on those of Si being etched.

The removal of deposited surfaces is also caused by physical sputtering through energetic  $\text{Cl}^+$  ion bombardment; in this study, the deposited  $\text{SiCl}_x$ ,  $\text{SiO}_y$ , and  $\text{SiCl}_x\text{O}_y$  are assumed to be desorbed or removed from the surface similarly to the situation of Eqs. (2), (3), and (10). It should be noted that the desorption angle of etch products from the surface being etched and the removal angle of etch products/byproducts from the surface deposited are all assumed to follow the cosine law for simplicity, as that for the surface re-emission or reflection of neutrals.

### III. RESULTS AND DISCUSSION

Input parameters for the profile simulation are a substrate temperature  $T_s$ , incoming flux  $\Gamma_{\text{O}}^0$  of O atoms from the

plasma onto substrate surfaces, sticking probability  $S_p$  of etch byproducts coming from the plasma, sticking probability  $S_q$  of etch products coming from feature surfaces, and returning probability  $P_r$  for the etch products. Here, the incoming flux of etch byproducts from the plasma onto substrate surfaces is given by  $\Gamma_p^0 = P_r \Gamma_q^s$  during main etch, where  $\Gamma_q^s$  is the flux of etch products that go out of the simulation domain or microstructural feature into the plasma. Note that during overetch time,  $\Gamma_p^0 = 0$  is given automatically because of  $\Gamma_q^s = 0$ . An incident  $\text{Cl}^+$  ion energy  $E_i = 50$  eV, ion temperature  $kT_i = 0.5$  eV ( $R = E_i/kT_i = 100$ ), incoming ion flux  $\Gamma_i^0 = 1.0 \times 10^{16} \text{ cm}^{-2} \text{ s}^{-1}$ , and incoming neutral reactant-to-ion flux ratio  $\Gamma_n^0/\Gamma_i^0 = 10$  onto substrate surfaces are fixed in this study, which are typical conditions in low-pressure, high-density plasmas such as electron cyclotron resonance<sup>6,39,40</sup> and inductively coupled plasmas. Moreover, the sticking probability  $S_n = 1$  is taken for Cl atoms or neutral reactants on unsaturated surfaces of Si, and the sticking probability  $S_{\text{O}} = 1$  is taken for O atoms on Si surfaces except for fully oxidized ones.

The initial surface profile is a mask pattern feature of lines and spaces on poly-Si films of thickness  $H_{\text{Si}} = 200$  nm. The mask pattern has a linewidth and height of  $L_{\text{mask}} = 100$  and  $H_{\text{mask}} = 100$  nm, respectively, each separated by six different spaces of width  $W = 30, 50, 70, 100, 200,$  and  $500$  nm. In addition, there is a  $\text{SiO}_2$  layer underlying the poly-Si, and the etching time is 200 s in the calculation. It is assumed that the mask and  $\text{SiO}_2$  are not eroded during etching, and that Cl and O neutrals are re-emitted thermally or reflected randomly thereon ( $S_n = S_{\text{O}} = 0$ ), where only the deposition of etch products/byproducts occurs. Note that the simulation domain concerned here is an area covering the whole of a series of line-and-space pattern features (not an area covering the respective pattern feature as shown in Fig. 1); in more detail, the simulation domain is taken to be  $\Delta x = 1550$  nm in width and  $\Delta z = 320$  nm in depth with periodic boundary conditions in the horizontal  $x$  axis, where the number of  $\text{Cl}^+$  ions successively injected is  $\Gamma_i^0 \Delta x \Delta y$  per unit time and that of Cl neutrals is  $\Gamma_n^0 \Delta x \Delta y$  ( $\Delta y = L$  as mentioned in Sec. II).

#### A. Ion-enhanced and spontaneous chemical etching

Figures 4(a)–4(c) show the etched profile evolution of line-and-space patterns of Si, simulated for different substrate temperatures  $T_s = 0, 300,$  and  $350$  K. The reaction probability given by Eq. (6) for chemical etching increases with increasing  $T_s$ , being  $\alpha_{\text{Si/Cl}} = 0, 0.001,$  and  $0.004$  at  $T_s = 0, 300,$  and  $350$  K, respectively. Calculations were performed without deposition of etch products/byproducts and surface oxidation ( $S_q = 0, \Gamma_p^0 = \Gamma_{\text{O}}^0 = 0$ ). In these figures, each curve represents the evolving interfaces obtained every 50 s, and insets are the respective vertical etch rates  $ER$  at the center of the  $W = 500$  nm feature bottom, which are almost the same as the etch rates for planar surfaces or open spaces.

At low  $T_s = 0$  K or without chemical etching, anisotropic profiles are achieved in the absence of undercutting on sidewalls, resulting from the ion-enhanced etching as in our previous study.<sup>17</sup> The etched profiles exhibit a little lateral etch-



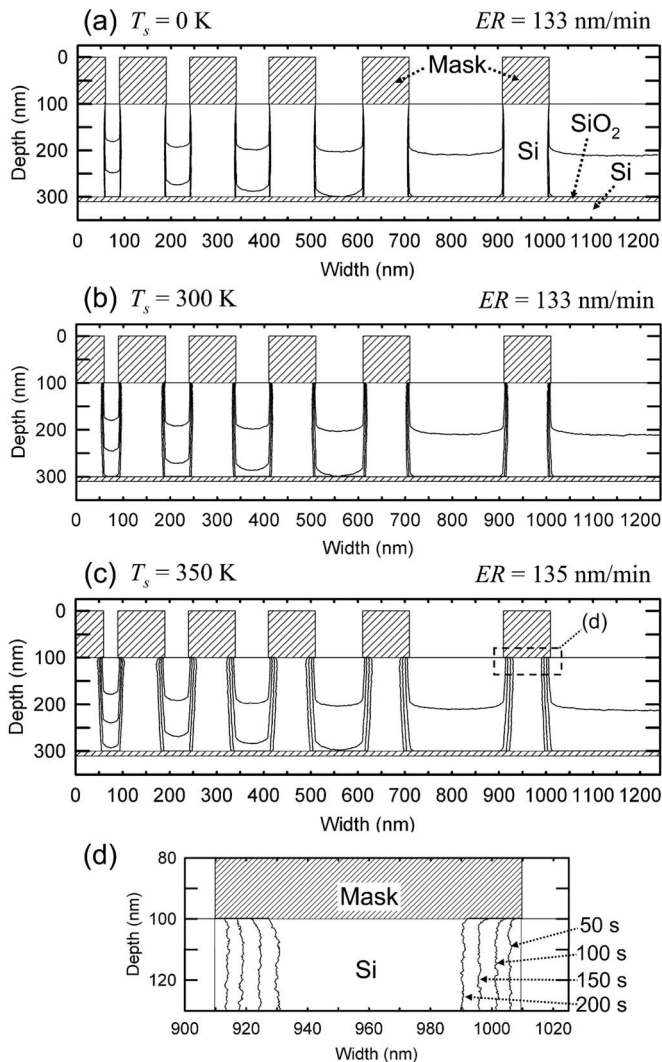


FIG. 4. Etched profile evolution of line-and-space patterns of Si for different substrate temperatures  $T_s$ =(a) 0, (b) 300, and (c) 350 K, simulated with an incident ion energy  $E_i=50$  eV, ion temperature  $kT_i=0.5$  eV ( $R=E_i/kT_i=100$ ), incoming ion flux  $\Gamma_i^0=1.0 \times 10^{16}$  cm $^{-2}$  s $^{-1}$ , and neutral reactant-to-ion flux ratio  $\Gamma_n^0/\Gamma_i^0=10$  onto substrate surfaces. The mask pattern has a linewidth and height of  $L_{\text{mask}}=100$  and  $H_{\text{mask}}=100$  nm, respectively, each separated by six different spaces of width  $W=30, 50, 70, 100, 200,$  and  $500$  nm. Note that the simulation domain concerned here is an area covering the whole of a series of line-and-space pattern features (not an area covering the respective pattern feature, as shown in Fig. 1). Calculations were performed without deposition of etch products/byproducts and surface oxidation ( $S_q=0, \Gamma_p^0=\Gamma_o^0=0$ ). Each curve represents the evolving interfaces obtained every 50 s, and insets are the respective vertical etch rates  $ER$  at the center of the  $W=500$  nm feature bottom, which are almost the same as the etch rates for planar surfaces or open spaces. Also shown is (d) the enlarged view of evolving interfaces beneath the mask for a line pattern between a space  $W=200$  and  $500$  nm, obtained every 50 s for  $T_s=350$  K.

ing on sidewalls owing to ions with off-normal incidence, and the round profiles at the feature bottom are caused by the geometrical shadowing for incoming ions and neutrals which reduces their fluxes incident on surfaces at around the corner of the bottom. Moreover, the etched profiles exhibit an RIE lag, where the etch rate or etched depth is smaller for narrower space features, because the neutral shadowing limits the flux of reactants of Cl incident on the bottom of the feature.<sup>41,42</sup>

The lateral etching or undercutting beneath the mask increases with increasing  $T_s$ , owing to the chemical etching effects enhanced. The lateral etch rate beneath the mask averaged over the period of  $t=50$ – $100$  s is  $0.5$ – $1$  and  $3$ – $5$  nm/min at  $T_s=300$  and  $350$  K, respectively, which is larger for wider space features owing to the neutral shadowing effects reduced. In contrast, the vertical etch rate remains almost unchanged by varying  $T_s$ , owing to the ion-enhanced etching at the feature bottom. However, the vertical etch rate is slightly smaller at higher  $T_s$  for narrow space features of  $W \leq 70$  nm, where a larger part of Cl neutrals tend to adsorb or stick and to be consumed on feature sidewalls in chemical etching, and thus the incident Cl flux is reduced on the bottom of the feature; as a result, the RIE lag is more significant at higher  $T_s$  for narrow features of  $W \leq 70$  nm.

Figure 4(d) shows the enlarged view of evolving interfaces beneath the mask for a line pattern between a space  $W=200$  and  $500$  nm, obtained every 50 s at  $T_s=350$  K. The lateral etch rate tends to be larger during overetch step ( $t > 90$  s) than during main etch because the Cl flux incident on feature sidewalls increases during overetch, owing to substantially decreased Cl neutrals that are consumed in the etching reaction at the bottom of the feature.

Figures 5(a) and 5(b) show the distribution of Cl atoms in Si substrates on sidewalls and bottom surfaces of the feature, respectively, for a  $W=500$  nm space at  $t=50$  s from the start of etching in the preceding Figs. 4(a)–4(c). Here, the depth is measured from the respective outermost surfaces, and the data shown are those averaged over  $125 \leq z \leq 175$  nm for sidewalls and over  $1200 \leq x \leq 1250$  nm for bottom surfaces. On feature sidewalls, most of Cl atoms are adsorbed or located on the outermost surfaces (or at the outermost surface cells or lattices), where the concentration ratio Cl/Si is  $\sim 4$ , corresponding to surfaces that are fully chlorine saturated. In contrast, at the bottom of the feature, Cl atoms are densely distributed over a depth of  $\sim 1$  nm, consisting of surface reaction multilayers formed through penetration of energetic Cl $^+$  ions into substrates during etching, which is consistent with the XPS analysis of chlorinated surfaces of Si etched in Cl $_2$  plasmas.<sup>43</sup> The concentration Cl/Si of  $\sim 3$  on the outermost bottom surfaces is smaller than that on feature sidewalls, because the surface coverage of chlorine is reduced at the feature bottom that is being etched under ion bombardment.

## B. Surface oxidation

Figures 6(a)–6(c) show the etched profile evolution of line-and-space patterns of Si, simulated for different incoming oxygen-to-ion flux ratios  $\Gamma_o^0/\Gamma_i^0=0.1, 0.5,$  and  $2.0$  at a substrate temperature  $T_s=300$  K [see Fig. 4(b) for  $\Gamma_o^0/\Gamma_i^0=0$ ]. Calculations were performed without deposition of etch products/byproducts ( $S_q=0, \Gamma_p^0=0$ ). Here, the graph properties are the same as those of Fig. 4. The etched profiles exhibit no undercutting beneath the mask, where the chemical etching is suppressed by surface oxidation on feature sidewalls. The etch rate decreases with increasing  $\Gamma_o^0/\Gamma_i^0$  owing to increased surface oxidation at the bottom of the fea-



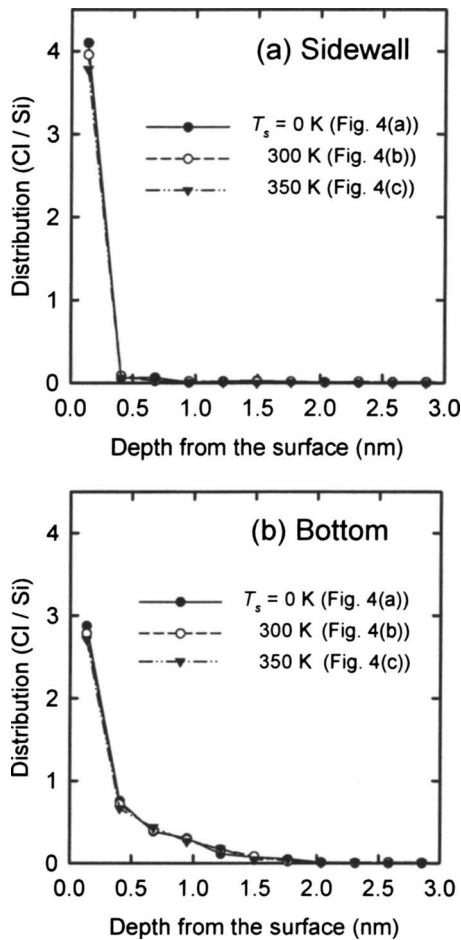


FIG. 5. Distribution of Cl atoms in Si substrates on (a) sidewalls and (b) bottom surfaces of the feature, for a  $W=500$  nm space at  $t=50$  s from the start of etching in the preceding Figs. 4(a)–4(c). Here, the depth is measured from the respective outermost surfaces, and the data shown are those averaged over  $125 \leq z \leq 175$  nm for sidewalls and over  $1200 \leq x \leq 1250$  nm for bottom surfaces.

ture, which is more significant for wider space features owing to the geometrical shadowing for incoming O neutrals. Thus, the RIE lag is reduced at increased  $\Gamma_O^0/\Gamma_i^0$ , and relatively uniform etch rates are achieved for different space features at  $\Gamma_O^0/\Gamma_i^0=2.0$ .

It should be noted here that at high  $\Gamma_O^0/\Gamma_i^0=0.5$  and 2.0, the etched profiles exhibit a weak inverse RIE lag for features in the range  $W=70$ –500 nm, where the etch rate or etched depth is slightly larger for narrower space features;<sup>40,44</sup> and a weak RIE lag remains for features in the range  $W=30$ –70 nm, owing to reduced fluxes of O atoms (or surface inhibitors) thereinto. Such a transition from regular to inverse RIE lag with increasing oxygen flux has been observed experimentally in Si etching with  $\text{Cl}_2/\text{O}_2$  plasmas;<sup>40</sup> in addition, the coexistence of RIE lag for narrow space features with inverse RIE lag for wider ones has also been observed in  $\text{SiO}_2$  etching with  $\text{CHF}_3$  plasmas.<sup>44</sup> Moreover, the round profiles at the feature bottom tend to be suppressed at increased  $\Gamma_O^0/\Gamma_i^0$  because the microscopically non-

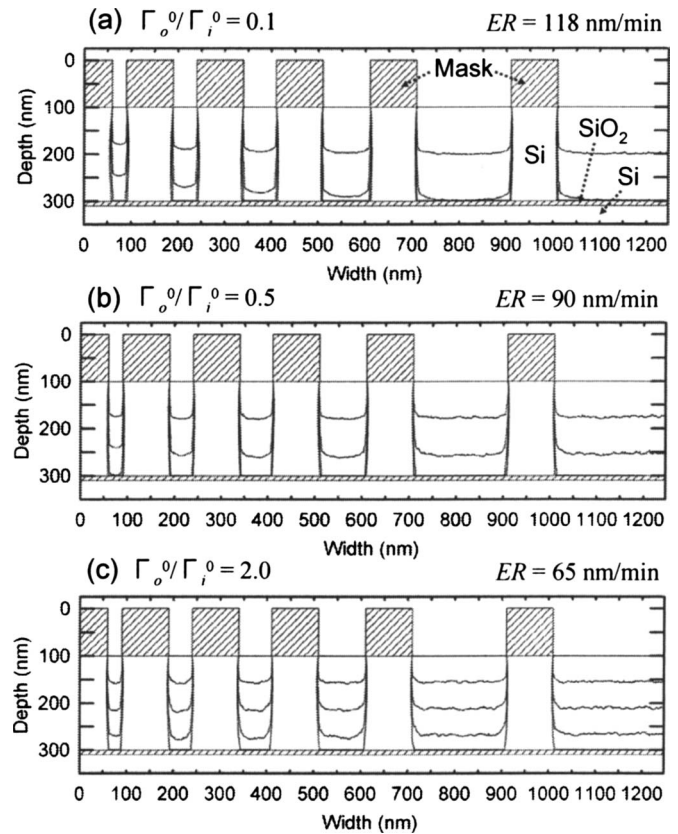


FIG. 6. Etched profile evolution of line-and-space patterns of Si, simulated for different incoming oxygen-to-ion flux ratios  $\Gamma_O^0/\Gamma_i^0=(a)$  0.1, (b) 0.5, and (c) 2.0 at a substrate temperature  $T_s=300$  K [see Fig. 4(b) for  $\Gamma_O^0/\Gamma_i^0=0$ ]. Calculations were performed without deposition of etch products/byproducts ( $S_p=0$ ,  $\Gamma_p^0=0$ ). Otherwise, the numerical conditions and graph properties are the same as those of Fig. 4.

uniform O flux incident on bottom surfaces leads to relatively large O coverage at the bottom center and thus to reduced etch rates thereat.

Figures 7(a)–7(d) show the distribution of Cl and O atoms in Si substrates on sidewalls and bottom surfaces of the feature, for a  $W=500$  nm space at  $t=50$  ns from the start of etching in the preceding Figs. 6(a)–6(c). Here, the graph properties are the same as those of Fig. 5. On feature sidewalls, most of Cl and O atoms are adsorbed or located on the outermost surfaces (or at the outermost surface cells or lattices), where the concentration ratio  $(\text{Cl}+\text{O})/\text{Si}$  of  $\sim 4$  remains unchanged by varying the oxygen flux  $\Gamma_O^0/\Gamma_i^0$ , corresponding to saturated surfaces with Cl and O; in practice, the O concentration relatively increases with increasing  $\Gamma_O^0/\Gamma_i^0$ . In contrast, at the bottom of the feature, Cl atoms are densely distributed over a depth of  $\sim 1$  nm, through penetration of energetic  $\text{Cl}^+$  ions into substrates during etching; the concentration  $(\text{Cl}+\text{O})/\text{Si}$  on the outermost bottom surfaces is  $\sim 3$  at low  $\Gamma_O^0/\Gamma_i^0=0.1$ , while increases to  $\sim 4$  at high  $\Gamma_O^0/\Gamma_i^0=2.0$  owing to increased surface oxidation. These are consistent with the XPS analysis of sidewall and bottom surfaces of Si etched in  $\text{Cl}_2/\text{O}_2$  plasmas.<sup>43</sup>

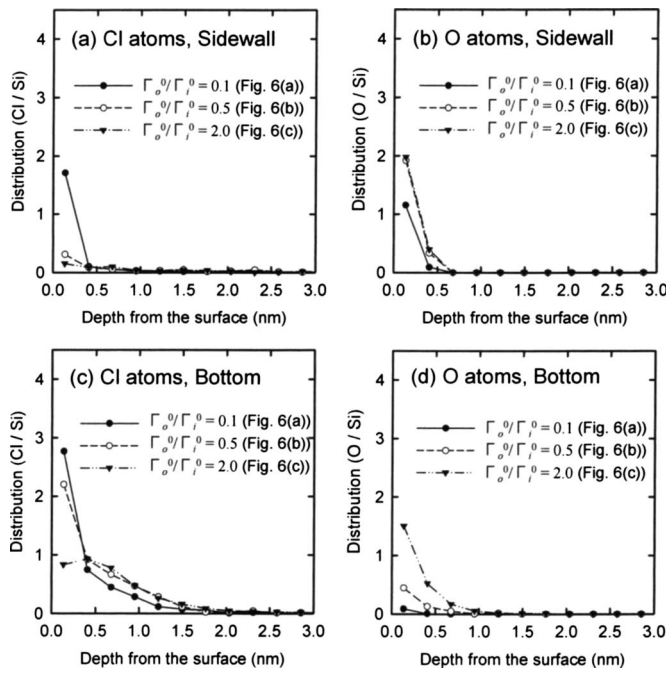


Fig. 7. Distribution of Cl and O atoms in Si substrates on (a) (b) sidewalls and (c) (d) bottom surfaces of the feature, for a  $W=500$  nm space at  $t=50$  s from the start of etching in the preceding Figs. 6(a)–6(c). Here, the graph properties are the same as those of Fig. 5.

### C. Redeposition of etch products desorbed from feature surfaces

#### 1. Without surface oxidation ( $\Gamma_p^0 = \Gamma_o^0 = 0$ )

Figures 8(a)–8(c) show the etched profile evolution of line-and-space patterns of Si, simulated for different sticking probabilities  $S_q=0.002, 0.02,$  and  $0.1$  of etch products desorbed or sputtered from feature surfaces during etching [see Fig. 4(b) for  $S_q=0$ ]. Each curve represents the evolving interfaces every 50 s, and insets are the respective vertical etch rates  $ER$  at the center of the  $W=500$  nm feature bottom. Calculations were made at a substrate temperature  $T_s=300$  K, without deposition of etch byproducts coming from the plasma and surface oxidation ( $\Gamma_p^0 = \Gamma_o^0 = 0$ ); thus, the etch products concerned here are silicon chlorides  $\text{SiCl}_x$  only. For small  $S_q=0.002$  as  $\text{SiCl}_4$ ,<sup>33</sup> nearly anisotropic profiles are obtained, where the chemical etching is suppressed by redeposition of etch products on feature sidewalls.

It should be noted here that for large  $S_q=0.02$  and  $0.1$  as unsaturated  $\text{SiCl}_x$ ,<sup>6,35</sup> the etched profiles exhibit sidewall tapering, which is more significant for larger  $S_q$ . The taper angle is increased deeper toward the bottom of the feature because the redeposition of etch products occurs more significantly on sidewalls near the feature bottom or the primary origin of products; moreover, the taper angle is larger or the redeposition is more significant for narrower space features, because of more frequent incidence of products on sidewalls therein, which has been observed experimentally in Si etching with  $\text{Cl}_2$  and  $\text{Cl}_2/\text{O}_2$  plasmas.<sup>40</sup> The etch rate is almost independent of  $S_q$  for wider features of  $W \geq 50$  nm, while it decreases significantly with increasing  $S_q$  for narrow features

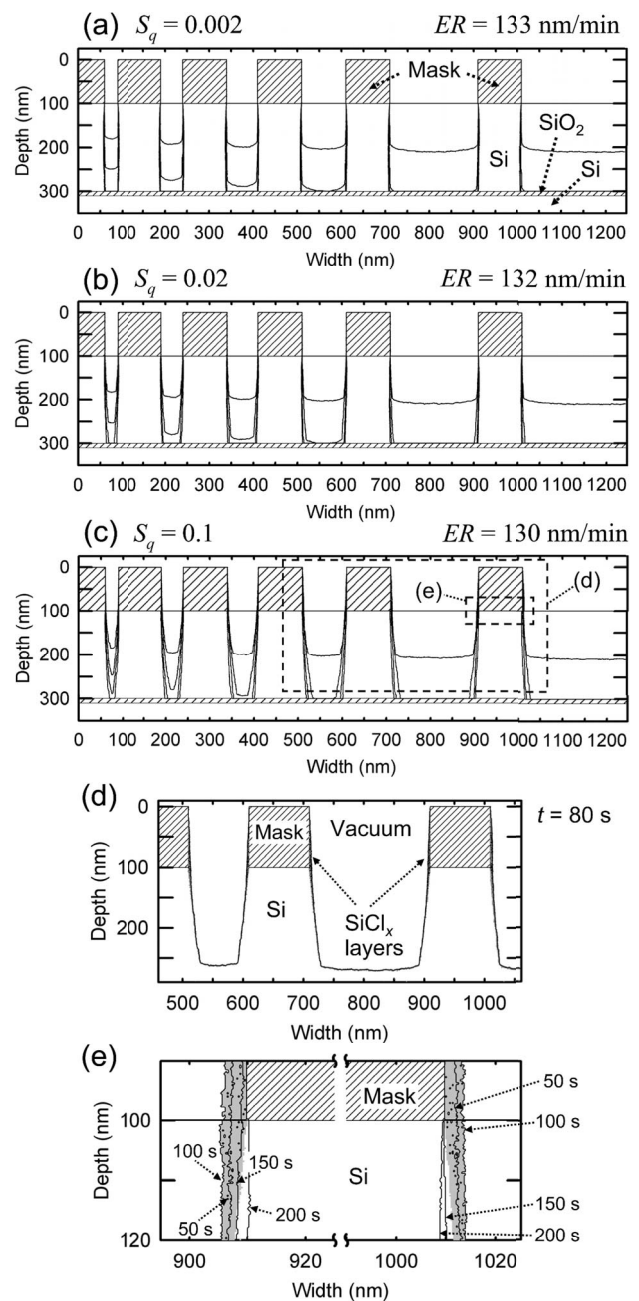


Fig. 8. Etched profile evolution of line-and-space patterns of Si, simulated for different sticking probabilities  $S_q=(a)$  0.002, (b) 0.02, and (c) 0.1 of etch products desorbed or sputtered from feature surfaces during etching [see Fig. 4(b) for  $S_q=0$ ]. Calculations were made at a substrate temperature  $T_s=300$  K, without deposition of etch byproducts coming from the plasma and surface oxidation ( $\Gamma_p^0 = \Gamma_o^0 = 0$ ); thus the etch products concerned here are silicon chlorides  $\text{SiCl}_x$  only. Otherwise, the numerical conditions and graph properties are the same as those of Fig. 4. Also shown are (d) a snapshot of the feature profile of lines and spaces for  $W=100, 200,$  and  $500$  nm, obtained at  $t=80$  s from the start of etching for  $S_q=0.1$ , and (e) the enlarged view of evolving interfaces on mask and Si sidewalls for a line pattern between a space  $W=200$  and  $500$  nm, obtained every 50 s for  $S_q=0.1$ . In (e), the shaded area corresponds to the  $\text{SiCl}_x$  layers deposited, and small blank areas therein represent a void or a region of cells or lattices without Si.

of  $W < 50$  nm, owing to significantly increased sidewall tapering therein. Thus, the degree of RIE lag remains almost unchanged by varying  $S_q$  for  $W \geq 50$  nm, while the RIE lag increased at increased  $S_q$  for  $W \leq 50$  nm.

Figure 8(d) shows a snapshot of the feature profile of lines and spaces for  $W=100, 200,$  and  $500$  nm, obtained at  $t=80$  s from the start of etching for  $S_q=0.1$ . The figure exhibits more clearly the sidewall tapering and etch rate (or etched depth) that depend on space feature width as described above. The  $\text{SiCl}_x$  layers deposited are formed on mask and Si sidewalls, and their thickness is maximum on mask sidewalls a little above the mask/Si interfaces, which is  $\sim 4$  nm on  $W=200$  nm feature sidewalls while  $\sim 3$  nm on  $W=500$  nm sidewalls. Figure 8(e) shows the enlarged view of evolving interfaces on mask and Si sidewalls for a line pattern between a space  $W=200$  and  $500$  nm, obtained every 50 s for  $S_q=0.1$ . In the figure, the shaded area corresponds to the  $\text{SiCl}_x$  layers deposited, and small blank areas therein represent a void or a region of cells or lattices without Si. The thickness of  $\text{SiCl}_x$  layers (or surface passivation layers) increases with time during etching at  $t \leq 90$  s, and then decreases with time during overetch ( $t > 90$  s) when the feature bottom reaches the underlying  $\text{SiO}_2$  layers and so the amount of etch products desorbed from feature surfaces is substantially decreased; in practice, at  $t \sim 150$  s, the  $\text{SiCl}_x$  layers on sidewalls are removed away by sputtering through ion bombardment, and then Si sidewalls are etched to become vertical.

## 2. With surface oxidation ( $\Gamma_{\text{O}}^0 \neq 0$ )

Figures 9(a)–9(c) show the etched profile evolution of line-and-space patterns of Si, simulated for different sticking probabilities  $S_q=0.002, 0.02,$  and  $0.1$  of etch products with further adding an incoming oxygen flux  $\Gamma_{\text{O}}^0/\Gamma_i^0=0.5$  to the situation of the preceding Figs. 8(a)–8(c) [see Fig. 6(b) for  $S_q=0$ ]. Note that calculations were made only without deposition of etch byproducts coming from the plasma ( $\Gamma_p^0=0$ ); thus, the etch products concerned here are  $\text{SiCl}_x, \text{SiO}_y,$  and/or  $\text{SiCl}_x\text{O}_y$  desorbed or sputtered from feature surfaces. The profile evolution in Fig. 9 exhibits the sidewall tapering similar to that in the preceding Fig. 8, which is caused by successive redeposition of etch products directly onto feature sidewalls during etching, being more significant for larger  $S_q$  and for narrower space features. It should be noted here that the sidewall tapering is significantly enhanced with surface oxidation for all space features investigated, which is also more significant for larger  $S_q$ . Moreover, the etch rate is significantly reduced with surface oxidation for all the features, which is also more significant for larger  $S_q$ . These are attributed to synergistic effects between the redeposition of etch products and surface oxidation, which enhance the formation of silicon oxychlorides  $\text{SiCl}_x\text{O}_y$  layers (or surface passivation layers) on feature sidewalls and bottom surfaces;<sup>45</sup> in practice, the synergistic effects occur for all the space features because the redeposition of etch products directly onto feature surfaces is more significant for narrower space features, while the oxygen flux onto feature surfaces is more significant for wider features owing to the geometrical shadowing for incoming O neutrals.

Moreover, the profile evolution in Fig. 9 also exhibits the dependence of the etch rate or etched depth on feature width

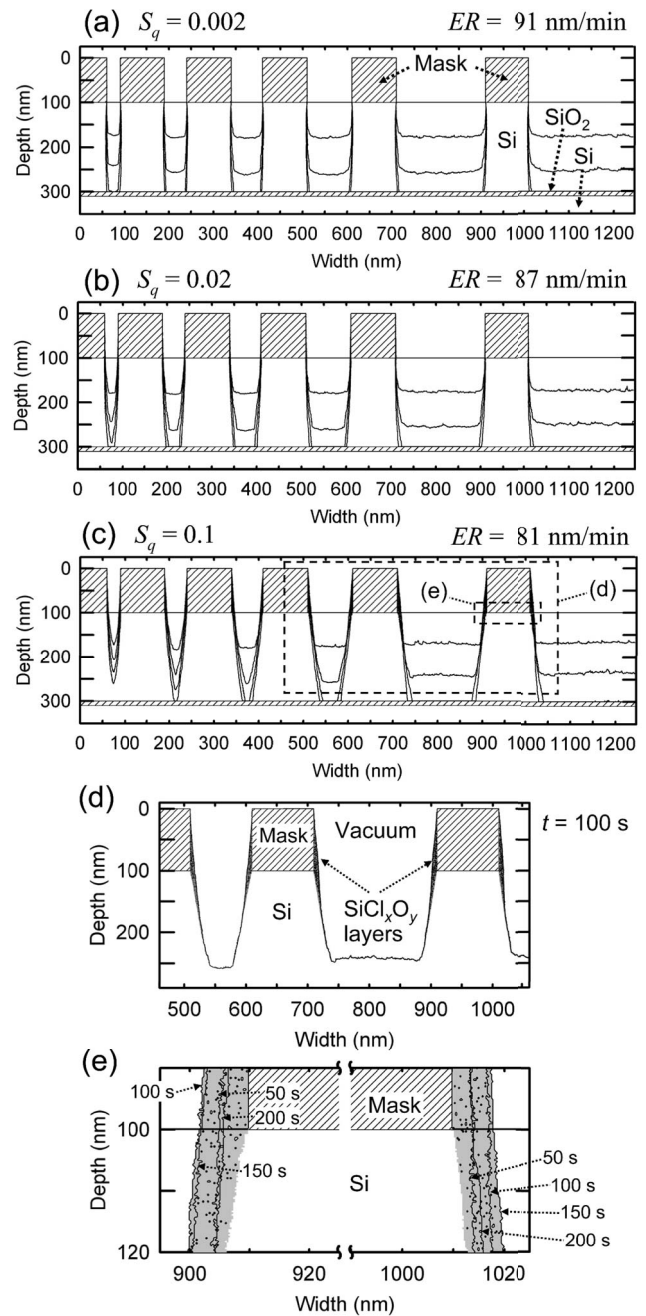


FIG. 9. Etched profile evolution of line-and-space patterns of Si, simulated for different sticking probabilities  $S_q=(a)$  0.002, (b) 0.02, and (c) 0.1 of etch products with further adding an incoming oxygen flux  $\Gamma_{\text{O}}^0/\Gamma_i^0=0.5$  to the situation of the preceding Figs. 8(a)–8(c) [see Fig. 6(b) for  $S_q=0$ ]. Calculations were made only without deposition of etch byproducts coming from the plasma ( $\Gamma_p^0=0$ ); thus the etch products concerned here are  $\text{SiCl}_x, \text{SiO}_y,$  and/or  $\text{SiCl}_x\text{O}_y$  desorbed or sputtered from feature surfaces. Otherwise, the numerical conditions and graph properties are the same as those of Fig. 4. Also shown are (d) a snapshot of the feature profile of lines and spaces for  $W=100, 200,$  and  $500$  nm, obtained at  $t=100$  s from the start of etching for  $S_q=0.1$ , and (e) the enlarged view of evolving interfaces on mask and Si sidewalls for a line pattern between a space  $W=200$  and  $500$  nm, obtained every 50 s for  $S_q=0.1$ . In (e), the graph properties are the same as those of the preceding Fig. 8(e).

similar to that in Fig. 6(b): an inverse RIE lag occurs for wider space features of  $W \geq 70$  nm, arising from surface oxi-



dation at the feature bottom through geometrical shadowing effects for incoming O neutrals; and an RIE lag is maintained for narrow features of  $W \leq 70$  nm, owing to reduced O fluxes therein. It should be noted here that owing to synergistic effects between the redeposition and surface oxidation, the inverse RIE lag with surface oxidation is more significant for larger  $S_q$ ; and the degree of RIE lag increased at increased  $S_q$  is more significant with surface oxidation. In practice, the reduction in the etch rate at the feature bottom with surface oxidation is more significant for wider space features, which is more significant for larger  $S_q$ ; and the reduction in the etch rate at increased  $S_q$  is more significant for narrower features owing to significantly increased sidewall tapering, which is more significant with surface oxidation.

Figure 9(d) shows a snapshot of the feature profile of lines and spaces for  $W=100, 200,$  and  $500$  nm, obtained at  $t=100$  s from the start of etching for large  $S_q=0.1$ . The figure exhibits more clearly the sidewall tapering and etch rate (or etched depth) that depend on space feature width as described above. The thickness of  $\text{SiCl}_x\text{O}_y$  layers formed on mask and Si sidewalls is increased with surface oxidation that occurs simultaneously with redeposition of etch products; their thickness is maximum on mask sidewalls a little above the mask/Si interfaces, which is  $\sim 8$  nm on  $W=200$  nm feature sidewalls while  $\sim 7$  nm on  $W=500$  nm sidewalls. Figure 9(e) shows the enlarged view of evolving interfaces on mask and Si sidewalls for a line pattern between a space  $W=200$  and  $500$  nm, obtained every 50 s for  $S_q=0.1$ . In the figure, the shaded area corresponds to the  $\text{SiCl}_x\text{O}_y$  layers formed, and small blank areas therein represent a void or a region of cells or lattices without Si, as in Fig. 8(e). The thickness of  $\text{SiCl}_x\text{O}_y$  or passivation layers increases with time during etching at  $t \leq 150$  s, and then decreases with time during overetch ( $t > 150$  s); in practice, at  $t \sim 200$  s, the  $\text{SiCl}_x\text{O}_y$  layers on sidewalls are not yet removed away by sputtering through ion bombardment, and so Si sidewalls are still being tapered.

## D. Deposition of etch byproducts coming from the plasma

### 1. Without surface oxidation ( $\Gamma_0^0=0$ )

Figures 10(a)–10(c) show the etched profile evolution of line-and-space patterns of Si, simulated for different returning probabilities  $P_r=0.2, 0.5,$  and  $1.0$  for the etch products that go out of the pattern feature into the plasma during etching [see Fig. 8(a) for  $P_r=0$  or  $\Gamma_p^0=0$ ]. Each curve represents the evolving interfaces every 50 s, and insets are the respective vertical etch rates  $ER$  at the center of the  $W=500$  nm feature bottom. Here, the respective probabilities  $P_r$  correspond to the ratios  $\Gamma_p^0/\Gamma_i^0 \approx 0.21, 0.51,$  and  $1.0$  of the etch byproduct to ion fluxes coming from the plasma onto substrate surfaces during main etch. Calculations were made at a substrate temperature  $T_s=300$  K, without only surface oxidation ( $\Gamma_0^0=0$ ) or with further adding incoming byproduct fluxes  $\Gamma_p^0/\Gamma_i^0$  during main etch to the situation of Fig. 8; thus, the etch products and byproducts concerned here are silicon chlorides  $\text{SiCl}_x$  only. The sticking probability was

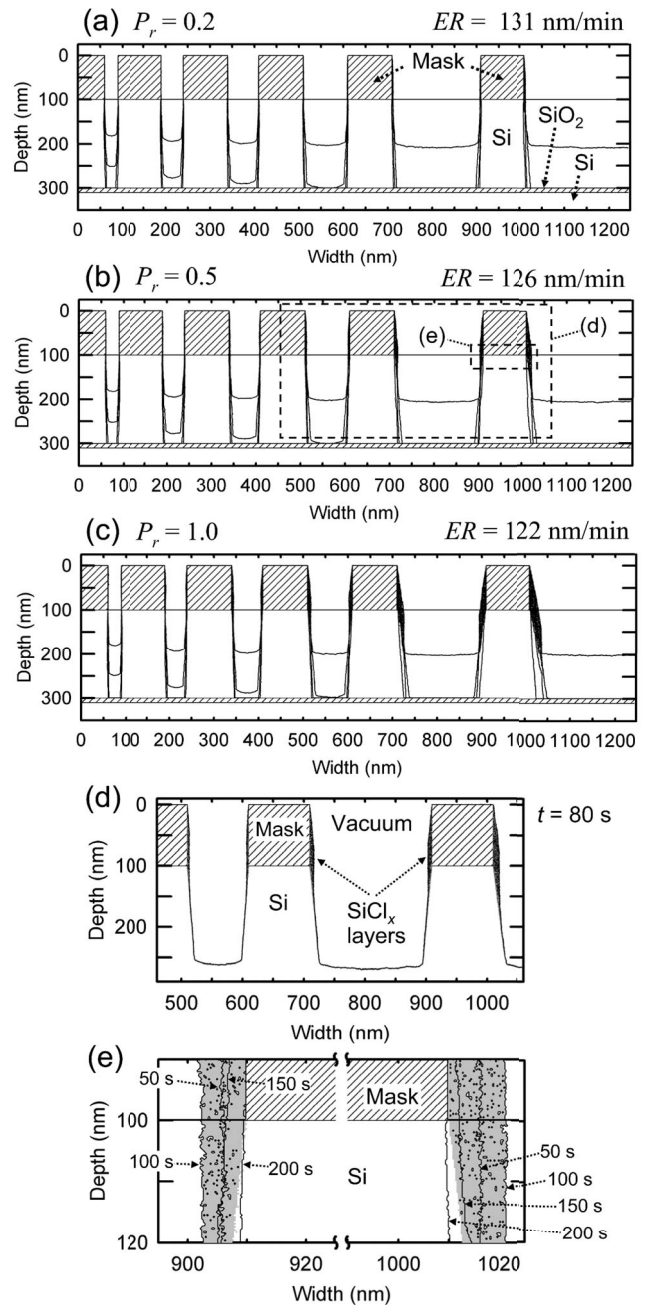


FIG. 10. Etched profile evolution of line-and-space patterns of Si, simulated for different returning probabilities  $P_r =$  (a) 0.2, (b) 0.5, and (c) 1.0 for the etch products that go out of the pattern feature into the plasma during etching [see Fig. 8(a) for  $P_r=0$  or  $\Gamma_p^0=0$ ]. Here, the respective probabilities  $P_r$  correspond to the ratios  $\Gamma_p^0/\Gamma_i^0 \approx 0.21, 0.51,$  and  $1.0$  of the etch byproduct to ion fluxes coming from the plasma onto substrate surfaces during main etch. Calculations were made at a substrate temperature  $T_s=300$  K, without only surface oxidation ( $\Gamma_0^0=0$ ) or with further adding incoming byproduct fluxes  $\Gamma_p^0/\Gamma_i^0$  during main etch to the situation of Fig. 8; thus, the etch products and byproducts concerned here are silicon chlorides  $\text{SiCl}_x$  only. The sticking probability was taken to be small or  $S_q=0.002$  [the same probability as in Fig. 8(a)] for etch products desorbed from feature surfaces, and to be large or  $S_p=0.1$  assuming  $\text{SiCl}_2$  for etch byproducts coming from the plasma. Otherwise, the numerical conditions and graph properties are the same as those of Fig. 4. Also shown are (d) a snapshot of the feature profile of lines and spaces for  $W=100, 200,$  and  $500$  nm, obtained at  $t=80$  s from the start of etching for  $P_r=0.5$ , and (e) the enlarged view of evolving interfaces on mask and Si sidewalls for a line pattern between a space  $W=200$  and  $500$  nm, obtained every 50 s for  $P_r=0.5$ . In (e), the graph properties are the same as those of the preceding Figs. 8(e) and 9(e).

taken to be small or  $S_q=0.002$  as  $\text{SiCl}_4$  [the same as in Fig. 8(a)] (Ref. 33) for etch products desorbed from feature surfaces, and to be large or  $S_p=0.1$  assuming  $\text{SiCl}_2$  (Ref. 6 and 35) for etch byproducts coming from the plasma. In this situation, effects of the redeposition of etch products are relatively small, and the deposition of silicon chlorides on feature sidewalls and bottom surfaces is dominated by that of byproducts from the plasma.

It should be noted here that the etched profiles exhibit the sidewall tapering that is enhanced with deposition of etch byproducts coming from the plasma, which is more significant for larger  $P_r$  or  $\Gamma_p^0/\Gamma_i^0$ . The taper angle is larger or the deposition is more significant for wider space features, owing to the geometrical shadowing for incoming etch byproducts (or surface inhibitors), which has been observed experimentally in Si etching with  $\text{Cl}_2$ ,<sup>40,45,46</sup>  $\text{Cl}_2/\text{O}_2$ ,<sup>40,45</sup>  $\text{HBr}$ ,<sup>46</sup> and  $\text{Cl}_2/\text{HBr}/\text{O}_2$ <sup>47,48</sup> plasmas. This is in contrast to the sidewall tapering caused by redeposition of etch products desorbed from feature surfaces, which is more significant for narrower features (see Fig. 8). Moreover, the etch rate decreases slightly with increasing  $P_r$  or  $\Gamma_p^0/\Gamma_i^0$ , owing to the deposition of byproducts onto the bottom of the feature, which is relatively significant for wide space features; thus, the degree of RIE lag is reduced a little at increased  $P_r$  or  $\Gamma_p^0/\Gamma_i^0$ . Note that the similar behavior of etched profiles is obtained through increasing the sticking probability  $S_p$  of etch byproducts for a given  $P_r$ .

Figure 10(d) shows a snapshot of the feature profile of lines and spaces for  $W=100, 200,$  and  $500$  nm, obtained at  $t=80$  s from the start of etching for middle  $P_r=0.5$ . The figure exhibits more clearly the sidewall tapering and etch rate (or etched depth) that depend on space feature width as described above. The  $\text{SiCl}_x$  layers deposited are formed on mask and Si sidewalls, and their thickness is maximum on mask sidewalls a little above the mask/Si interfaces, decreasing toward Si sidewalls. These are consistent with the experiments of Si etching in  $\text{Cl}_2$ ,<sup>45</sup>  $\text{Cl}_2/\text{O}_2$ ,<sup>45</sup> and  $\text{Cl}_2/\text{HBr}/\text{O}_2$  (Refs. 48 and 49) plasmas, and with a discussion regarding the facet angle of deposited films and taper angle of sidewalls during etching.<sup>11,50,51</sup> The maximum thickness of  $\text{SiCl}_x$  layers in the figure is  $\sim 7$  nm on  $W=200$  nm feature sidewalls while  $\sim 10$  nm on  $W=500$  nm sidewalls. Figure 10(e) shows the enlarged view of evolving interfaces on mask and Si sidewalls for a line pattern between a space  $W=200$  and  $500$  nm, obtained every 50 s for  $P_r=0.5$ . In the figure, the shaded area corresponds to the  $\text{SiCl}_x$  layers deposited, and small blank areas therein represent a void or a region of cells or lattices without Si, as in Figs. 8(e) and 9(e). The thickness of  $\text{SiCl}_x$  or passivation layers increases with time during etching at  $t \leq 90$  s, and then decreases with time during overetch ( $t > 90$  s) when the feature bottom reaches the underlying  $\text{SiO}_2$  layers and so the amount of etch products desorbed from feature surfaces and thus etch byproducts coming from the plasma is substantially reduced; in practice, at  $t \sim 200$  s, the  $\text{SiCl}_x$  layers on sidewalls are removed away by sputtering through ion bombardment, and then Si sidewalls are etched to become vertical.

## 2. With surface oxidation ( $\Gamma_0^0 \neq 0$ )

Figures 11(a)–11(c) show the etched profile evolution of line-and-space patterns of Si, simulated for different returning probabilities  $P_r=0.2, 0.5,$  and  $1.0$  with further adding an incoming oxygen flux  $\Gamma_0^0/\Gamma_i^0=0.5$  to the situation of the preceding Figs. 10(a)–10(c) [see Fig. 9(a) for  $P_r=0$  or  $\Gamma_0^0=0$ ]. Here, the respective probabilities  $P_r$  correspond to the ratios  $\Gamma_p^0/\Gamma_i^0 \approx 0.16, 0.39,$  and  $0.60$  during main etch. Note that the values of  $\Gamma_p^0/\Gamma_i^0$  are smaller than those in Fig. 10, because of the etch rates decreased owing to surface oxidation. Calculations were made with all the effects concerned in this study; thus, the etch products concerned here are  $\text{SiCl}_x$ ,  $\text{SiO}_y$ , and/or  $\text{SiCl}_x\text{O}_y$  desorbed or sputtered from feature surfaces, having a sticking probability  $S_q=0.002$ . Moreover, the etch byproducts coming from the plasma are assumed to be  $\text{SiCl}_2\text{O}$  having a sticking probability  $S_p=0.1$ .

The profile evolution in Fig. 11 exhibits the sidewall tapering similar to that in the preceding Fig. 10: the tapering is caused by successive deposition of etch byproducts from the plasma onto feature sidewalls during etching, being more significant for larger  $P_r$  or  $\Gamma_p^0/\Gamma_i^0$  and for wider space features. It is noted here that the sidewall tapering is slightly reduced with surface oxidation owing to decreased  $\Gamma_p^0/\Gamma_i^0$ , which is in contrast to the effects of oxidation on the profile evolution with redeposition of etch products (see Figs. 8 and 9); however, if we compare the sidewall tapering with and without surface oxidation in case of similar values of  $\Gamma_p^0/\Gamma_i^0$ , the tapering is slightly enhanced with oxidation, which is more significant for larger  $\Gamma_p^0/\Gamma_i^0$  and for wider space features. Moreover, the etch rate is reduced with surface oxidation, as in Fig. 9, which is also more significant for larger  $P_r$  or  $\Gamma_p^0/\Gamma_i^0$  and for wider space features. These are attributed to synergistic effects between the deposition of etch byproducts and surface oxidation, which enhance the formation of silicon oxychlorides  $\text{SiCl}_x\text{O}_y$  layers (or surface passivation layers) on feature sidewalls and bottom surfaces;<sup>45</sup> in practice, the synergistic effects are more significant for wider space features, because of the geometrical shadowing for etch byproducts and oxygen coming from the plasma onto feature surfaces.

Moreover, the profile evolution in Fig. 11 also exhibits the dependence of the etch rate or etched depth on feature width similar to that in Fig. 9 [and also Fig. 6(b)]: an inverse RIE lag occurs for wider space features of  $W \geq 70$  nm, while an RIE lag is maintained for narrow features of  $W \leq 70$  nm. It should be noted here that owing to synergistic effects between the deposition and surface oxidation which are both more significant for wider space features, the inverse RIE lag with surface oxidation is more significant for larger  $P_r$  or  $\Gamma_p^0/\Gamma_i^0$ ; and the degree of RIE lag slightly decreased at increased  $P_r$  or  $\Gamma_p^0/\Gamma_i^0$  is less significant with surface oxidation. In addition, for large  $P_r=1.0$  or  $\Gamma_p^0/\Gamma_i^0=0.60$ , the increased surface roughness occurs at the bottom of the wide space feature of  $W=500$  nm, which is caused by micromasks formed through the deposition of etch byproducts enhanced with surface oxidation during etching. This is considered to correspond to the situation which often occurs in Si etching



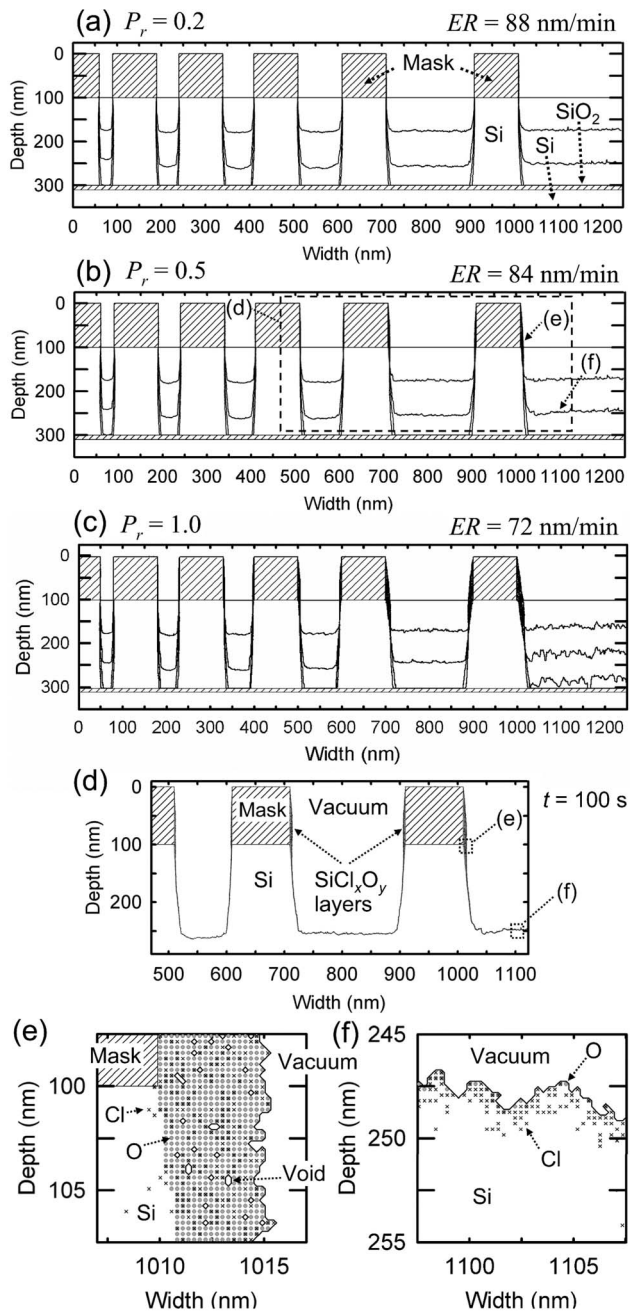


FIG. 11. Etched profile evolution of line-and-space patterns of Si, simulated for different returning probabilities  $P_r$ =(a) 0.2, (b) 0.5, and (d) 1.0 with further adding an incoming oxygen flux  $\Gamma_{O_i}^0/\Gamma_i^0=0.5$  to the situation of the preceding Figs. 10(a)–10(c) [see Fig. 9(a) for  $P_r=0$  or  $\Gamma_{O_i}^0=0$ ]. Here, the respective probabilities  $P_r$  correspond to the ratios  $\Gamma_{O_i}^0/\Gamma_i^0 \approx 0.16, 0.39,$  and  $0.60$  during main etch. Calculations were made with all the effects concerned in this study; thus, the etch products concerned here are  $\text{SiCl}_x$ ,  $\text{SiO}_y$ , and/or  $\text{SiCl}_x\text{O}_y$  desorbed or sputtered from feature surfaces, having a small sticking probability  $S_q=0.002$ . Moreover, the etch byproducts coming from the plasma were assumed to be  $\text{SiCl}_2\text{O}$  having a large sticking probability  $S_p=0.1$ . Otherwise, the numerical conditions and graph properties are the same as those of Fig. 4. Also shown are (d) a snapshot of the feature profile of lines and spaces for  $W=100, 200,$  and  $500$  nm, obtained at  $t=100$  s from the start of etching for  $P_r=0.5$ , and the enlarged or microscopic view of (e) sidewall and (f) bottom surface layers for  $P_r=0.5$ , together with the distribution of Cl and O atoms therein. In (e) (f), the crosses and solid gray circles represent cells or lattices with not only Si but also Cl and O atoms adsorbed, respectively; and small blank areas represent a void or a region of cells or lattices without Si as in the preceding Figs. 8(e), 9(e), and 10(e).

with  $\text{Cl}_2/\text{O}_2$  plasmas at high  $\text{O}_2$  flow rates, leading to significantly reduced etch rates along with rough surfaces.<sup>30</sup>

Figure 11(d) shows a snapshot of the feature profile of lines and spaces for  $W=100, 200,$  and  $500$  nm, obtained at  $t=100$  s from the start of etching for middle  $P_r=0.5$ . The figure exhibits more clearly the sidewall tapering and etch rate (or etched depth) that depend on space feature width as described above. The thickness of  $\text{SiCl}_x\text{O}_y$  layers formed on mask and Si sidewalls is decreased with surface oxidation that occurs simultaneously with deposition of etch byproducts; their thickness is maximum on mask sidewalls a little above the mask/Si interfaces, which is  $\sim 3.5$  nm on  $W=200$  nm feature sidewalls while  $\sim 5$  nm on  $W=500$  nm sidewalls.

Figures 11(e) and 11(f) show the enlarged or microscopic view of sidewall and bottom surface layers, respectively, for  $P_r=0.5$ , together with the distribution of Cl and O atoms therein. Here, the crosses and solid gray circles represent cells or lattices with not only Si but also Cl and O atoms adsorbed, respectively, and small blank areas represent a void or a region of cells or lattices without Si, as in Figs. 8(e), 9(e), and 10(e). On feature sidewalls, the  $\sim 5$ -nm-thick  $\text{SiCl}_x\text{O}_y$  or passivation layers contain densely distributed O and relatively sparse Cl atoms, being attributed to strongly reactive O neutrals which displace Cl adsorbed, as mentioned earlier [Eq. (9)]. In contrast, at the bottom of the feature, Cl atoms are densely distributed over a depth of  $>1$  nm, which form  $\text{SiCl}_x$  or reaction multilayers on substrate surfaces; in practice, Cl neutrals adsorbed on bottom surfaces are desorbed as etch products under continuous bombardment of energetic ions thereon [Eqs. (2), (3), and (10)], and so the adsorbed Cl atoms shown originate primarily from energetic  $\text{Cl}^+$  ions penetrating into substrates during etching. There are only a few O atoms adsorbed or located on the outermost surfaces (or at the outermost surface cells or lattices) because they are also desorbed or sputtered continuously through ion bombardment [Eq. (10)].

Figures 12(a) and 12(b) show the distribution of Si, Cl, and O atoms in  $\text{SiCl}_x\text{O}_y$  or passivation layers on mask and Si sidewalls of the feature, respectively, for a  $W=500$  nm space at  $t=100$  ns from the start of etching with  $P_r=0.5$  in Fig. 11(d). Also shown in Fig. 12(c) is the distribution in  $\text{SiCl}_x$  or reaction multilayers on bottom surfaces in the same situation. In the figure, the thickness on sidewalls in (a) and (b) is measured from the position of initial mask sidewall surfaces, and the depth on bottom surfaces in (c) is measured from the outermost surfaces; the data shown are those averaged over  $80 \leq z \leq 100$  nm in (a) and  $110 \leq z \leq 130$  nm in (b) for sidewalls, and over  $1060 \leq x \leq 1090$  nm in (c) for bottom surfaces. These figures exhibit more clearly the distribution of Cl and O atoms on feature surfaces as described above. On mask sidewalls in (a), the thickness of  $\text{SiCl}_x\text{O}_y$  layers is  $\sim 5$  nm, containing densely distributed O and relatively sparse Cl atoms, where the concentration ratio is  $(\text{Cl} + 2\text{O})/\text{Si} \sim 4$ , corresponding to saturated surfaces with Cl and O. On Si sidewalls in (b), the thickness of  $\text{SiCl}_x\text{O}_y$  layers is relatively thin of  $\sim 3$  nm, containing also densely distrib-



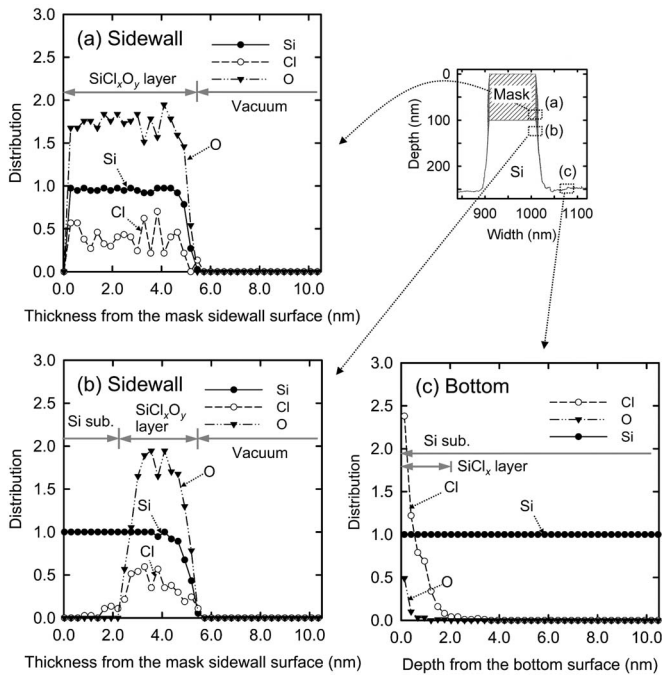


FIG. 12. Distribution of Si, Cl, and O atoms in  $\text{SiCl}_x\text{O}_y$  or passivation layers on (a) mask and (b) Si sidewalls of the feature, for a  $W=500$  nm space at  $t=100$  ns from the start of etching with  $P_r=0.5$  in the preceding Fig. 11(d). Also shown in (c) is the distribution in  $\text{SiCl}_x$  or reaction multilayers on bottom surfaces in the same situation. Here, the thickness on sidewalls in (a) and (b) is measured from the position of initial mask sidewall surfaces, and the depth on bottom surfaces in (c) is measured from the outermost surfaces; the data shown are those averaged over  $80 \leq z \leq 100$  nm in (a) and  $110 \leq z \leq 130$  nm in (b) for sidewalls, and over  $1060 \leq x \leq 1090$  nm in (c) for bottom surfaces.

uted O and relatively sparse Cl atoms with the concentration ratio being  $(\text{Cl}+2\text{O})/\text{Si} \sim 4$ . In contrast, at the bottom of the feature, Cl atoms are densely distributed over a depth of  $\sim 1$  nm, through penetration of energetic  $\text{Cl}^+$  ions into substrates during etching, where the concentration  $(\text{Cl}+2\text{O})/\text{Si}$  on the outermost surfaces is  $\sim 3.5$ . The concentration of Cl and O atoms on feature sidewalls and bottom surfaces is similar to that shown in Fig. 7, being consistent with the experiments of Si etching in  $\text{Cl}_2/\text{O}_2$  plasmas.<sup>43</sup>

#### IV. CONCLUSIONS

Atomic-scale cellular model has been developed to simulate the feature profile evolution during poly-Si gate etching in high-density  $\text{Cl}_2$  and  $\text{Cl}_2/\text{O}_2$  plasmas, including the formation of passivation layers on feature surfaces. Emphasis was placed on a deeper understanding of plasma-surface interactions during etching, to achieve nanometer-scale control of the etched profile, CD, and their microscopic uniformity (or aspect-ratio dependence). The model took into account  $\text{Cl}^+$  ions, Cl and O neutrals, and etch byproducts of  $\text{SiCl}_x$  and  $\text{SiCl}_x\text{O}_y$  coming from the plasma into microstructural features; moreover, etch products such as  $\text{SiCl}_x$  and  $\text{SiCl}_x\text{O}_y$  were taken to be desorbed or sputtered from feature surfaces. The transport of ions and neutrals in microstructure was analyzed by using a two-dimensional particle simulation based

on successively injected single-particle trajectories with three velocity components; moreover, the Monte Carlo calculation was employed for the trajectory of ions penetrating into substrates. The surface chemistry included ion-enhanced etching, spontaneous chemical etching, and passivation layer formation through surface oxidation and deposition of etch products and byproducts. To incorporate an atomistic picture into the model, the computational domain of infinitely long trenches was taken to consist of two-dimensional square cells or lattices of atomic size, and the evolving interfaces were represented by removing Si atoms from and/or allocating them at the respective cells concerned.

Calculations were performed for different line-and-space pattern features of down to 30 nm space width, with an incoming ion energy, ion flux, and neutral reactant-to-ion flux ratio of  $E_i=50$  eV,  $\Gamma_i^0=1.0 \times 10^{16}$   $\text{cm}^{-2}$   $\text{s}^{-1}$ , and  $\Gamma_n^0/\Gamma_i^0=10$ . Numerical results reproduced the evolution of feature profiles, CDs, and their microscopic uniformity on nanometer scale, depending on substrate temperature, incoming flux of oxygen and etch byproducts, and sticking probability of etch products and byproducts on feature surfaces: the lateral etching on sidewalls is suppressed by surface oxidation thereon. The oxidation also reduces the etch rate on bottom surfaces, which is more significant for wider space features, thus leading to a transition from regular to inverse RIE lag with increasing flux of oxygen; in practice, the RIE lag remains almost unchanged for narrow space features owing to reduced oxygen fluxes thereinto, thus leading to regular and inverse RIE lags coexistent in a series of different pattern features. The deposition or redeposition of etch products (desorbed from feature surfaces) onto sidewalls results in the sidewall tapering, which is more significant for narrower space features; in contrast, the deposition of byproducts (coming from the plasma) onto sidewalls results in the tapering, which is more significant for wider features. Synergistic effects between the deposition of etch products/byproducts and surface oxidation enhance the passivation layer formation on feature surfaces, which in turn increases the sidewall tapering and the degree of regular and inverse RIE lags depending on feature width. The present model also enabled us to simulate the surface reaction multilayers and passivation layers on atomic scale, along with their chemical constituents and surface roughness.

Further studies are now in progress for the present atomic-scale model of the etched profile evolution during poly-Si gate etching in  $\text{Cl}_2/\text{HBr}/\text{O}_2$  and  $\text{HBr}/\text{O}_2$  as well as  $\text{Cl}_2/\text{O}_2$  plasmas, further taking into account the reflection of energetic ions on feature surfaces and the mask erosion. A comparison with experiments is also now in progress, to gain a better understanding of competitive and/or synergistic plasma-surface interactions during etching, which play a key role in suppressing nanometer-scale profile anomalies and thus in achieving the nanometer-scale control of etched profiles, CDs, and their microscopic uniformity in advanced gate etch processes.

## ACKNOWLEDGMENTS

This work was supported in part by a Grant-in-Aid for Scientific Research from the Japan Society for the Promotion of Science, and in part by the 21st Century Center of Excellence (COE) program of the Ministry of Education, Culture, Sports, Science and Technology. The authors would like to thank Shoki Irie for assistance with profile simulation.

- <sup>1</sup>E. Pargon, M. Darnon, O. Joubert, T. Chevolleau, L. Vallier, L. Mollard, and T. Lill, *J. Vac. Sci. Technol. B* **23**, 1913 (2005).
- <sup>2</sup>K. V. Guinn and V. M. Donnelly, *J. Appl. Phys.* **75**, 2227 (1994).
- <sup>3</sup>K. V. Guinn, C. C. Cheng, and V. M. Donnelly, *J. Vac. Sci. Technol. B* **13**, 214 (1995).
- <sup>4</sup>F. H. Bell and O. Joubert, *J. Vac. Sci. Technol. B* **14**, 2493 (1996).
- <sup>5</sup>F. H. Bell and O. Joubert, *J. Vac. Sci. Technol. B* **15**, 88 (1997).
- <sup>6</sup>K. Nishikawa, T. Oomori, and K. Ono, *J. Vac. Sci. Technol. B* **17**, 127 (1999).
- <sup>7</sup>M. Tuda, K. Ono, and K. Nishikawa, *J. Vac. Sci. Technol. B* **14**, 3291 (1996).
- <sup>8</sup>M. Tuda, K. Nishikawa, and K. Ono, *J. Appl. Phys.* **81**, 960 (1997).
- <sup>9</sup>R. J. Hoekstra, M. J. Grapperhaus, and M. J. Kushner, *J. Vac. Sci. Technol. A* **15**, 1913 (1997).
- <sup>10</sup>A. P. Mahorowala and H. H. Sawin, *J. Vac. Sci. Technol. B* **20**, 1064 (2002).
- <sup>11</sup>A. P. Mahorowala and H. H. Sawin, *J. Vac. Sci. Technol. B* **20**, 1077 (2002).
- <sup>12</sup>M. E. Barone and D. B. Graves, *J. Appl. Phys.* **78**, 6604 (1995).
- <sup>13</sup>D. E. Hanson, A. F. Voter, and J. D. Kress, *J. Appl. Phys.* **82**, 3552 (1997).
- <sup>14</sup>H. Ohta and S. Hamaguchi, *J. Vac. Sci. Technol. A* **19**, 2373 (2001).
- <sup>15</sup>D. Humbird and D. B. Graves, *J. Appl. Phys.* **96**, 791 (2004).
- <sup>16</sup>A. Sano, K. Ono, K. Takahashi, and Y. Setsuhara, in *Proceedings of the Second International Symposium on Dry Process (DPS 2002)*, Tokyo, 2002 (IEEJ, Tokyo, 2002), pp. 177–182.
- <sup>17</sup>Y. Osano and K. Ono, *Jpn. J. Appl. Phys., Part 1* **44**, 8650 (2005).
- <sup>18</sup>R. A. Gottscho, *J. Vac. Sci. Technol. B* **11**, 1884 (1993).
- <sup>19</sup>J. F. Ziegler, J. P. Biersack, and U. Littmark, *The Stopping and Range of Ions in Solids* (Pergamon, New York, 1985).
- <sup>20</sup>M. Tanaka, T. Shirao, T. Sakai, K. Shudo, H. Washio, and N. Kaneko, *J. Vac. Sci. Technol. A* **20**, 1358 (2002).
- <sup>21</sup>M. Tanaka, E. Yamakawa, T. Shirao, and K. Shudo, *Phys. Rev. B* **68**, 165411 (2003).
- <sup>22</sup>D. J. D. Sullivan, H. C. Flaum, and A. C. Kummel, *J. Phys. Chem.* **97**, 12051 (1993).
- <sup>23</sup>H. C. Flaum, D. J. D. Sullivan, and A. C. Kummel, *J. Phys. Chem.* **98**, 1719 (1994).
- <sup>24</sup>J. P. Chang, A. P. Mahorowala, and H. H. Sawin, *J. Vac. Sci. Technol. A* **16**, 217 (1998).
- <sup>25</sup>S. Tachi, K. Tsujimoto, S. Arai, and T. Kure, *J. Vac. Sci. Technol. A* **9**, 796 (1991).
- <sup>26</sup>E. A. Ogryzlo, D. E. Ibbotson, D. L. Flamm, and J. A. Mucha, *J. Appl. Phys.* **67**, 3115 (1990).
- <sup>27</sup>M. Lieberman and A. Lichtenberg, *Principles of Plasma Discharges and Materials Processing* (Wiley Interscience, New York, 1994).
- <sup>28</sup>J. R. Engstrom and T. Engel, *Phys. Rev. B* **41**, 1038 (1990).
- <sup>29</sup>J. R. Engstrom, M. M. Nelson, and T. Engel, *J. Vac. Sci. Technol. A* **7**, 1837 (1989).
- <sup>30</sup>T. Morimoto, *Jpn. J. Appl. Phys., Part 1* **32**, 1253 (1993).
- <sup>31</sup>L. Desvoivres, L. Vallier, and O. Joubert, *J. Vac. Sci. Technol. B* **19**, 420 (2001).
- <sup>32</sup>D. J. Oostra, R. P. van Ingen, A. Haring, A. E. de Vries, and G. N. A. van Veen, *Appl. Phys. Lett.* **50**, 1506 (1987).
- <sup>33</sup>L. J. Whitman, S. A. Joyce, J. A. Yarmoff, F. R. McFeely, and L. J. Terminello, *Surf. Sci.* **232**, 297 (1990).
- <sup>34</sup>P. Gupta, P. A. Coon, B. G. Koehler, and S. M. George, *J. Chem. Phys.* **93**, 2827 (1990).
- <sup>35</sup>T. Sakai, A. Sakai, and H. Okano, *Jpn. J. Appl. Phys., Part 1* **32**, 3089 (1993).
- <sup>36</sup>V. M. Donnelly, *J. Appl. Phys.* **79**, 9353 (1996).
- <sup>37</sup>C. Lee, D. B. Graves, and M. A. Lieberman, *Plasma Chem. Plasma Process.* **16**, 99 (1996).
- <sup>38</sup>R. N. Tait, T. Smy, and M. J. Brett, *Thin Solid Films* **187**, 375 (1990).
- <sup>39</sup>K. Ono, M. Tuda, K. Nishikawa, T. Oomori, and K. Namba, *Jpn. J. Appl. Phys., Part 1* **33**, 4424 (1994).
- <sup>40</sup>M. Tuda and K. Ono, *Jpn. J. Appl. Phys., Part 1* **36**, 2482 (1997).
- <sup>41</sup>R. A. Gottscho, C. W. Jurgensen, and D. J. Vitkavage, *J. Vac. Sci. Technol. B* **10**, 2133 (1992).
- <sup>42</sup>A. D. Bailey III, M. C. M. van de Sanden, J. A. Gregus, and R. A. Gottscho, *J. Vac. Sci. Technol. B* **13**, 92 (1995).
- <sup>43</sup>N. Layadi, V. M. Donnelly, and T. C. Lee, *J. Appl. Phys.* **81**, 6738 (1997).
- <sup>44</sup>M. F. Doemling, N. R. Rueger, and G. S. Oehrlein, *Appl. Phys. Lett.* **68**, 10 (1996).
- <sup>45</sup>Y. Osano, M. Mori, N. Itabashi, K. Takahashi, K. Eriguchi, and K. Ono, *Jpn. J. Appl. Phys., Part 1* **45**, 8157 (2006).
- <sup>46</sup>A. P. Mahorowala, H. H. Sawin, R. Jones, and A. H. Labun, *J. Vac. Sci. Technol. B* **20**, 1055 (2002).
- <sup>47</sup>M. Tuda, K. Shintani, and H. Ootera, *J. Vac. Sci. Technol. A* **19**, 711 (2001).
- <sup>48</sup>X. Detter, R. Palla, I. Thomas-Boutherin, E. Pargon, G. Cunge, O. Joubert, and L. Vallier, *J. Vac. Sci. Technol. B* **21**, 2174 (2003).
- <sup>49</sup>M. Tuda, K. Shintani, and J. Tanimura, *Plasma Sources Sci. Technol.* **12**, S72 (2003).
- <sup>50</sup>V. Vahedi, J. Daugherty, S. Huang, D. Cooperberg, R. A. Gottscho, H. J. Tao, H. J. Lin, C. S. Tsai, and M. S. Liang, in *Proceedings of the 21st Symposium on Dry Process (DPS 1999)*, Tokyo, 1999 (IEEJ, Tokyo, 1999).
- <sup>51</sup>D. J. Cooperberg, V. Vahedi, and R. A. Gottscho, *J. Vac. Sci. Technol. A* **20**, 1536 (2002).